

---

---

# University of Bristol Thesis Template

*Subtitle*

---

---

By

AUTHOR'S NAME



Department of Engineering Mathematics  
UNIVERSITY OF BRISTOL

A dissertation submitted to the University of Bristol in accordance with the requirements of the degree of DOCTOR OF PHILOSOPHY in the Faculty of Engineering.

APRIL 2013

Word count: ten thousand and four



## **ABSTRACT**

**H**ere goes the abstract



## **DEDICATION AND ACKNOWLEDGEMENTS**

**H**ere goes the dedication.



## AUTHOR'S DECLARATION

I declare that the work in this dissertation was carried out in accordance with the requirements of the University's Regulations and Code of Practice for Research Degree Programmes and that it has not been submitted for any other academic award. Except where indicated by specific reference in the text, the work is the candidate's own work. Work done in collaboration with, or with the assistance of, others, is indicated as such. Any views expressed in the dissertation are those of the author.

SIGNED: ..... DATE: .....



## TABLE OF CONTENTS

	<b>Page</b>
<b>List of Tables</b>	<b>ix</b>
<b>List of Figures</b>	<b>xi</b>
<b>1 Introduction</b>	<b>1</b>
1.1 Evidence for the Existence Of Dark Matter . . . . .	1
1.1.1 Virial Theorem . . . . .	2
1.1.2 Galactic Rotation Curves . . . . .	2
1.1.3 Gravitational Lensing . . . . .	3
1.1.4 Cosmic Microwave Background . . . . .	4
1.2 Particle Candidates and Other Solutions to the Dark Matter Problem . . . . .	6
1.2.1 Axions . . . . .	6
1.2.2 Primordial Black Holes . . . . .	7
1.3 Non Linear Emission of Radiation in Liquid Xenon . . . . .	7
1.4 EFT . . . . .	9
<b>2 Effective Field Theory Search For High Energy Nuclear Recoils in XENON100 Detector</b>	<b>11</b>
2.1 Low energy channel . . . . .	12
2.2 High energy channel . . . . .	13
2.3 Signal model . . . . .	15
2.3.1 Elastic scattering . . . . .	16
2.3.2 Inelastic WIMP scattering . . . . .	18
2.4 Statistical inference . . . . .	18
2.5 Data From Recoil Energies Up To 1000 PE . . . . .	20
2.6 Results . . . . .	21
2.7 Summary . . . . .	23
<b>3 Direxeno</b>	<b>25</b>
<b>4 Calibration System for Xenon1T</b>	<b>27</b>

TABLE OF CONTENTS

---

4.1 Radioactive source . . . . .	28
4.1.1 ER band calibration . . . . .	28
4.1.2 Charge collection efficiency . . . . .	31
4.2 Collimators . . . . .	31
4.2.1 Simulation . . . . .	32
4.2.2 First Results . . . . .	34
<b>A EFT SIGNAL MODEL DETECTOR RESPONSE TABLE</b>	<b>37</b>
<b>Bibliography</b>	<b>41</b>

## LIST OF TABLES

<b>TABLE</b>	<b>Page</b>
2.1 Definitions and contents of the analysis bins for the high energy channel. The expected background counts are calculated by taking the calibration sample and scaling it by $6.54 \times 10^{-3}$ , which is the ratio of observed counts to calibration counts in a sideband.	<a href="#">15</a>
4.1 High energy gamma lines from $^{228}\text{Th}$ decay chain . . . . .	<a href="#">30</a>
4.2 result of GEANT4 simulations for a 16X16X16cm collimator with an aperture of 45 deg, a good event is an event that scattered only once in the FV with energy deposition of 2-15 keVee . . . . .	<a href="#">34</a>
4.3 result of GEANT4 simulation for a 10X10X10cm collimator with an aperture of 45 deg, a good event is an event that scattered only once in the FV with energy deposition of 2-15 keVee . . . . .	<a href="#">35</a>
A.1 Detector response table using $\mathcal{L}_{\text{eff}}$ with constrained scaling parameter set to $-1\sigma$ value. First column gives recoil energies, subsequent columns give the values of $G'_i(E)$ for each of the 9 high-energy analysis bins. The sampling is in steps of 10 keV <sub>nr</sub> , which is too coarse to give an accurate signal model for very low WIMP masses, but is suitable for the mass range most relevant to our analysis. Higher resolution $G'_i(E)$ functions, and $G'_i(E)$ functions for other values of $\mathcal{L}_{\text{eff}}$ , are given in supplementary material. . . . .	<a href="#">38</a>



## LIST OF FIGURES

<b>FIGURE</b>	<b>Page</b>
1.1 Rotation curve of NGC 6503. . . . .	3
1.2 (a) Hubble Space Telescope Advanced Camera for Surveys image of the lensing cluster Abell 1689. Image credit: ESA/Hubble. (b) QSO-2237 quasar lensed image, creating both einstein's arcs and cross. Image credit: CASTLES . . . . .	4
1.3 Bullet Cluster . . . . .	5
1.4 Plank 2015 CMB power spectrum . . . . .	6
1.5 TODO list of figures caption. . . . .	8
2.1 Summary of regions of interest, backgrounds, and observed data. ER calibration data, namely $^{60}\text{Co}$ and $^{232}\text{Th}$ data is shown as light cyan dots. NR calibration data ( $^{241}\text{AmBe}$ ) is shown as light red dots. Dark matter search data is shown as black dots. The red line is the threshold between the low and high energy channels. The lines in blue are the bands. For the low-energy channel the bands are constructed to achieve constant expected signal density, and are operator and mass dependent, shown here for a $50 \text{ GeV}/c^2$ WIMP using the $\mathcal{O}_1$ operator. For the high-energy region, the nine analysis bins are presented also in blue lines. . . . .	12
2.2 The total acceptance of all cuts used. Data from calibration is shown in black, with a 3rd order polynomial fit in red. . . . .	14
2.3 The expected signal in the high energy region for a $300 \text{ GeV}/c^2$ WIMP mass, normalized to 5 events. Left(right) is the spectra for $O_1(O_6)$ . Notice that for $O_1$ most of the events are not expected to deposit energy higher than 30 PE whereas for $O_6$ a large fraction of the events appear in this region. . . . .	17
2.4 The expected signal in the low energy region for a $300 \text{ GeV}/c^2$ WIMP mass, normalized to 5 events. Left(right) is the spectra for $\mathcal{O}_1(\mathcal{O}_6)$ . Notice that for $\mathcal{O}_1$ most of the events are expected to deposit energy lower than 30 PE whereas for $\mathcal{O}_6$ a large fraction of the events do not appear in this region at all. The black lines indicate the bands constructed on these specific mass and operator models, and are dividing the signal into 8 equally distributed signal sub-regions. This parameter space can be mapped with a one to one mapping to the $(y - cS1)$ space. . . . .	17

---

LIST OF FIGURES

2.5	The full XENON100 dark matter science run data up to 1000 PE in cS1 (shown in black). In blue we show data from ER calibration ( $^{60}\text{Co}$ and $^{232}\text{Th}$ ) and in red from NR calibration ( $^{241}\text{AmBe}$ ). See text for details on these populations. While the black vertical line represents the highest energy considered for quantitative interpretation in this analysis, there is no indication of elastic NRs even above that energy. . . . .	20
2.6	The XENON100 limits (90% CL <sub>S</sub> ) on isoscalar dimensionless coupling for all elastic scattering EFT operators. The limits are indicated in solid black. The expected sensitivity is shown in green and yellow(1 $\sigma$ and 2 $\sigma$ respectively). Limits from CDMS-II Si, CDMS-II Ge, and SuperCDMS [1] are presented as blue asterisks, green triangles, and orange rectangles, respectively. For operator 3 and 8 a full limit was published, for all other operators only $m_\chi = 10$ and $m_\chi = 300$ are available. . . . .	22
2.7	90% CL <sub>S</sub> limits, for the inelastic model, on the magnitude of the coupling constant for $\mathcal{O}_1$ , reported as a function of the WIMP mass and mass splitting $\delta$ . . . . .	23
2.8	The XENON100 90% CL <sub>S</sub> limits on a 1 TeV/ $c^2$ WIMP isoscalar dimensionless coupling constant as function of the WIMP mass splitting $\delta_m$ for all inelastic scattering EFT operators. Limits are indicated in solid black. The expected sensitivity is shown in green and yellow (1 $\sigma$ and 2 $\sigma$ respectively). For $\mathcal{O}_1$ (SI) results from XENON100(red triangle) CDMS-II(blue rectangle) and ZEPLIN-III(black star) are overlaid. . . . .	24
4.1	Attenuation coefficient of Xe. The relevant density for LXe is 3 g/cc. . . . .	29
4.2	$^{228}\text{Th}$ decay chain . . . . .	30
4.3	$^{137}\text{Cs}$ decay . . . . .	31
4.4	(a) The cryostat and the collimator shining just some of the FV (b) a CAD design of the collimator with the conical hole. . . . .	32
4.5	A picture of the two belts. The blue belt is the I-Belt (currently not the I-Belt in use). The grey belt is the U-Belt (with the U-Collimator mounted), which passes below the cryostat. . . . .	33
4.6	A top view of the water tank . . . . .	33
4.7	(a) scatter of good calibration events in the SV, the red line is the border of the FV (b) Intial momentum of background events i.e., events which trigger PMT's and do not meet all three conditions, FV, single scattered, and energy deposition range . . . . .	34
4.8	(a) scatter of good calibration events in the SV, the red line is the border of the FV (b) Intial momentum of background events i.e., events which trigger PMT's and do not meet all three conditions, FV, single scattered, and energy deposition range . . . . .	35





## INTRODUCTION

The most accredited theoretical framework for the cosmology of our universe, based on numerous cosmological and astronomical observations, is the "Λ-Cold Dark Matter" model (Λ-CDM). It suggests that only a small fraction (~ 5%) of the energy density in the universe is in the form of baryonic matter, the rest ~ 95% is lurking in the dark [2, 3]. The "Dark-sector" consist of *Dark Energy*(~ 69%) and a non-baryonic matter (~ 26%), *Dark Matter* (DM).

In the 1930s the Swiss astronomer Fritz Zwicky observed that the mass of the cluster inferred by gravitational observation is much larger than the one inferred by the visible luminous light matter. He then deduced the existence of a new type of unseen matter which does not interact with electromagnetic radiation, naming this matter "*dunkle materie*", *Dark Matter* [4]. Since then much evidence has been accumulated, suggesting that DM is present at galactic as well as cosmological scales.

In the past decade many experiments joined the hunt for DM detection, and the field has progressed dramatically. These experiments can be divided roughly into three groups, underground direct detection experiments such as XENON [5, 6], LUX [7], PANDAX [8], CDMS [9], DAMA/LIBRE [10] and others , indirect detection in space (FERMI [11], AMS [12]) and on earth (IceCube [13]), and production experiments in accelerators such as ATLAS [14] and CMS [15] at the Large Hadron Collider.

### 1.1 Evidence for the Existence Of Dark Matter

An extensive amount of observations pointing to the presence of DM at the single galaxy, intergalactic and cosmological scales, are present. In this section a brief summary of these observation is presented.

### 1.1.1 Virial Theorem

The virial theorem relates the average potential energy density  $\langle V_p \rangle$  of a stationary gravitationally bound system to its mean kinetic energy density  $\langle T_k \rangle$ , namely:

$$(1.1) \quad \langle T_k \rangle = -\frac{1}{2} \langle V_p \rangle.$$

In the 1930s Zwicky made the puzzling observation that the velocity dispersion of individual nebulae in the large Coma galaxy cluster contradicts the expectation of the virial theorem, if estimating the total mass solely from the visible matter content [4]. Additional mass in the form of DM needs to be added to explain the observations. Although Zwicky did not take into account the mass of the hot plasma in the cluster, adding it reduces the discrepancies but doesn't solve it.

The hot plasma bounded by the gravitational potential of the cluster emits bremsstrahlung X-rays. The x-ray emission is proportional to the plasma density squared. This can be used to estimate the the total mass and mass profile of clusters assuming the cluster is virialized. This type of observations suggest that DM rather than baryonic matter dominates the dynamics of clusters [? ].

### 1.1.2 Galactic Rotation Curves

The orbital velocity as a function of radius (rotation curve) can be obtained from the measurement of the redshifts of the 1420 MHz hydrogen transition [16] as well as of spectral lines from stars. The hydrogen cloud extends beyond the galactic disk, allowing the measurement of orbital velocities further out. By measuring the rotation curve of galaxies it is possible to compute their mass profile ( $M(r)$ ).

In 1970 Vera Rubin found a disagreement in the mass profile calculated by the rotation curves and the one expected from luminous matter in NGC4605 spiral galaxy [17]. This disagreement can be solved, assuming additional non-visible mass enhancing the gravitational forces.

Formally, assuming Newtonian dynamics

$$(1.2) \quad v(r) = \sqrt{\frac{G \cdot M(r)}{r}},$$

where

$$(1.3) \quad M(r) = \int_0^r 4\pi\rho(r)r^2 dr.$$

The majority of a galaxy's luminous mass is situated at the close vicinity of its center ; therefore if no other mass exist, at large radii one would expect  $v(r) \sim r^{-1/2}$ . In contradiction the measurements done by Rubin and in many more experiments indicate  $v(r) \sim \text{const}$ , see Fig ???. Adding DM with density profile  $\rho(r) \sim r^{-2}$  explains this observations.

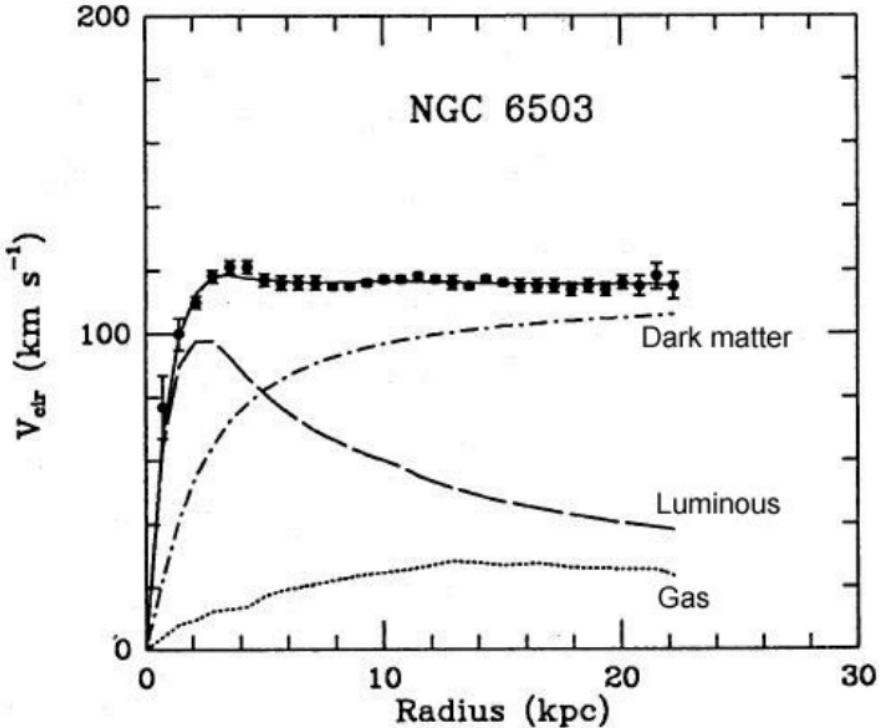


FIGURE 1.1. Measured Rotation curve (solid line) of NGC 6503 galaxy. In dashed, luminous component only. In dotted, the gas component, and expected DM halo in dotted-dashed. Image taken from [16].

### 1.1.3 Gravitational Lensing

One of the predictions of general relativity is that trajectory of light in space is determined by the space-time metric, which is determined by the mass distribution. Due to this effect, when a large gravitational potential is located in the line of sight between an observer and a far galaxy, the light from the galaxy is distorted. This phenomena is called Gravitational Lensing [18]. By analyzing the lensed image, the mass profile of the "lens" can be characterized.

*Strong Lensing* is when the gravitational field of the "lens" is so strong it produces multiple images forming an Einstein's cross, as well as Einstein's rings [19]. In Fig. 1.2(a) is a picture of the largest lensing galaxy cluster observed, Abell 1689. In Fig. 1.2(b) is the a lensed, multiple image picture of the quasar QSO-2237.

Two important features are concuded when analyzing the mass profile of the "lens": 1) DM and ordinary matter are not misaligned [20]. 2) The mass profile follows  $\rho(r) \propto r^{-2}$  dispersion ratio [21].

*Weak Lensing* is when the light coming from the source is only weakly distorted by the gravitational lens. In this case it is impossible to detect an individual lensed source; however, multiple background sources align symmetrically around the lens, allowing the detection of the

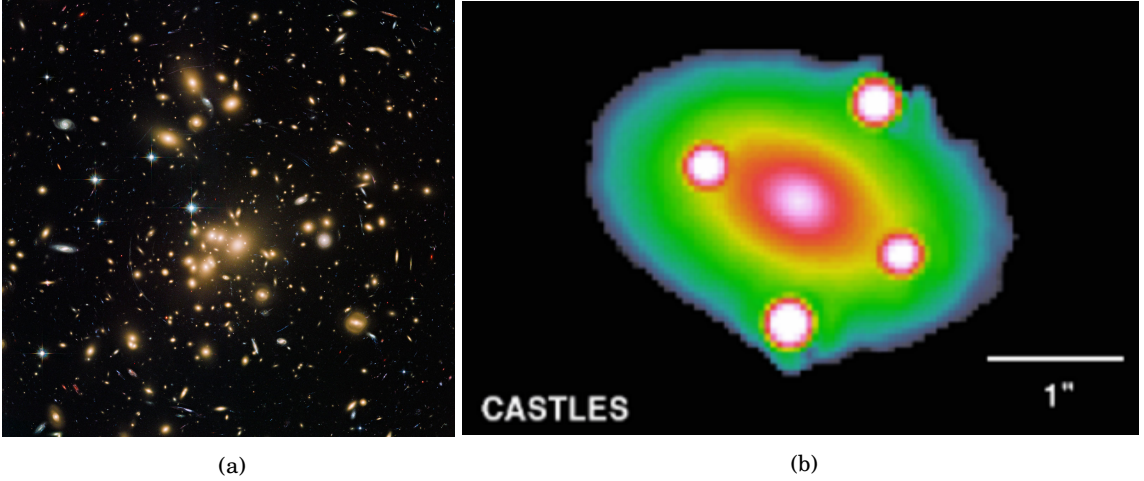


Figure 1.2: (a) Hubble Space Telescope Advanced Camera for Surveys image of the lensing cluster Abell 1689. Image credit: ESA/Hubble. (b) QSO-2237 quasar lensed image, creating both einstein's arcs and cross. Image credit: CASTLES

lens mass [22].

The most famous weak lensing evidence for DM comes from the "Bullet Cluster", a lensed image of a collision of two galaxies, 1E0657-56 and MACS J0025.4-1222 [23]. In this observation (see Fig. ??), it is clear that the mass distribution of the luminous and non-luminous matters are spatially displaced. While the luminous matter seems to experienced a violent collision, the non-luminous matter seems to be unaffected. The collisionless behaviour of the DM puts strong constrains on its self interaction [24].

#### 1.1.4 Cosmic Microwave Background

The most precise constraint of the abundance of dark matter in the Universe and a landmark test on the  $\Lambda$ -CDM model comes from the measurements of the cosmic microwave background (CMB). The CMB is a remnant thermal electromagnetic radiation field from the early Universe.

At the early stages of the Universe, it was hot, dense, and filled with plasma. Then after expanding enough the temperature dropped, and electrons and protons recombined creating hydrogen atoms. At that stage (referred as "recombination time"), as the density of free electrons dropped, the thermal radiation could travel freely, without being scattered. These photons propagate through the Universe ever since.

The CMB follows with extreme precision the spectrum of a black body with temperature of 2.726 K. It is also known to be very isotropic and temperature anisotropy is at the scale of  $10\mu\text{K}$ . These temperature fluctuations, considered Gaussian [2], are usually expanded using spherical

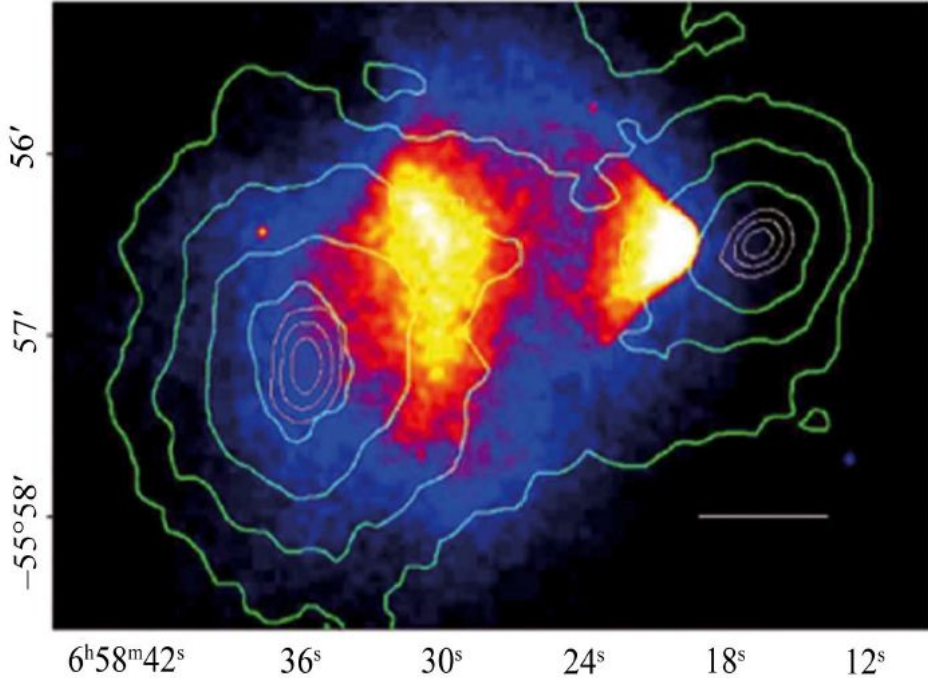


FIGURE 1.3. Contours of spatial distribution of mass, from gravitational lensing overplotted over Chandra x-ray data that traces hot plasma in a galaxy. It can be seen that most of the matter resides in a location different from the plasma, which underwent frictional interactions during the merger and slowed down.

harmonics,

$$(1.4) \quad \frac{\delta T}{T}(\theta, \phi) = \sum_{l=2}^{\infty} \sum_{m=-l}^{m=l} a_{lm} Y_{lm}(\theta, \phi).$$

The variance of the coefficient  $a_{lm}$  denoted as  $c_l$  is defined:

$$(1.5) \quad c_l \equiv \langle a_{lm} \rangle = \frac{1}{2l+1} \sum_{m=-l}^{m=l} a_{lm}^2$$

All DM relevance information from CMB can be extracted from the power spectrum of  $C_l$  as a function of the multipole  $l$ . The shape of the power spectrum follows the oscillations of the plasma in the early Universe. In general, the flatness of the Universe can be extracted from the position of the first peak. The ratio between the baryonic and non-baryonic matter is extracted from the ratio between the first 2 peaks.

More specifically, there are many parameters which affect the CMB spectrum, amongst them are the DM density ( $\Omega_{DM}$ ), the baryonic matter density ( $\Omega_b$ ) and the Hubble constant ( $h$ ). Assuming a cosmological model with fixed number of parameters the best fit to the spectrum determines the values of the parameters. The most updated measurement of the CMB spectrum seen in Fig 1.4 constrains the values of the above mentioned parameters [3] to:

$$(1.6) \quad \Omega_{DM} h^2 = 0.1197 \pm 0.0022 \quad \Omega_b h^2 = 0.00222 \pm 0.00023 \quad h = 0.67 \text{ [100 km/s/Mpc]}$$

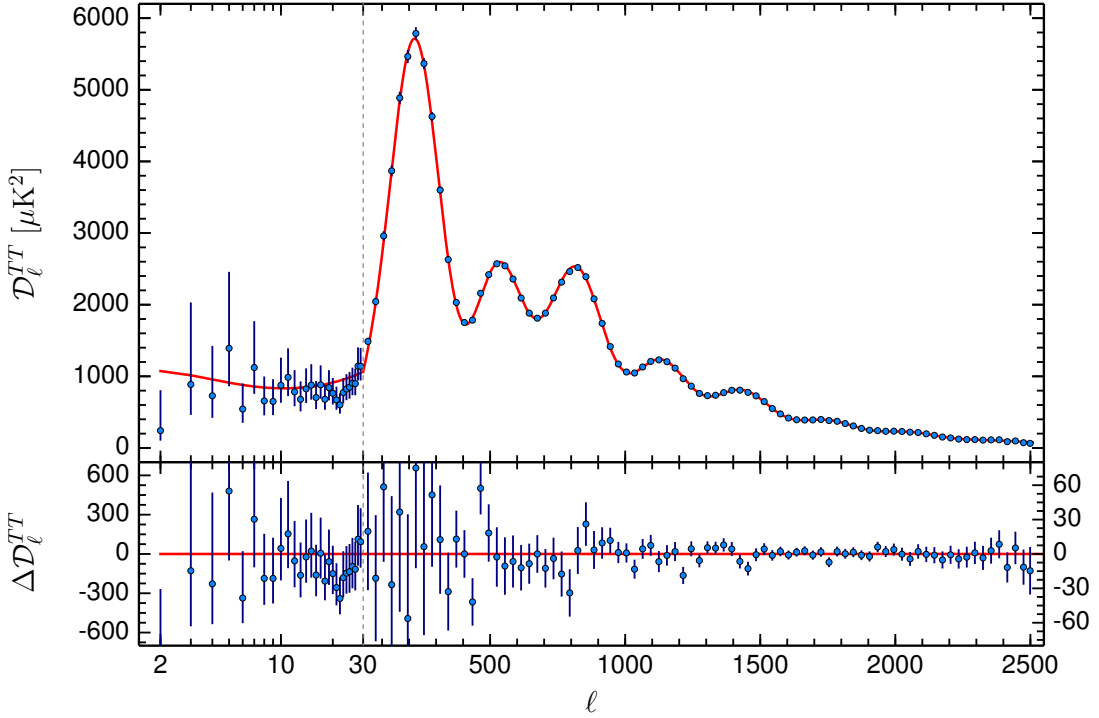


FIGURE 1.4. The Planck 2015 temperature power spectrum the solid line is the best fit for the  $\Lambda$ -CDM model, the error bars show  $\pm\sigma$  uncertainties

## 1.2 Particle Candidates and Other Solutions to the Dark Matter Problem

As discussed in previous section there is a large number of convincing evidences for supporting the existence of DM in the Universe, of which its nature is yet unknown. In this section is a short discussion of possible candidates for DM particles, as well as an alternative solution involving the modification of Newton's laws.

### 1.2.1 Axions

Axions are neutral pseudoscalars initially introduced by Peccei and Quinn in 1977 to solve the "strong CP problem" [25]. The Standard model of particles (SM) contains a CP violating proportional to the parameter  $\bar{\theta} = \theta_{weak} + arg(det(M))$ . From measurements of the electrical dipole moment of the neutron the  $\bar{\theta}$  parameter is constrained to be smaller than  $10^{-10}$  [26, 27]. The question why the  $\bar{\theta}$  parameter is so small is known as the strong CP problem. An elegant

solution to this problem is introducing an additional global  $U(1)$  symmetry, spontaneously broken producing a Goldstone boson known as the axion.

Many theoretical and experimental efforts were invested in axion search. The original proposed Peccei-Quinn axion with symmetry breaking scale in the order of the weak scale ( $10^{-23}$  GeV) is ruled out; however, axion and axion like particles (ALPs) are still allowed [28]. For current experimental limits on axions and ALPs see [29]

### 1.2.2 Primordial Black Holes

## 1.3 Non Linear Emission of Radiation in Liquid Xenon

As explained in ( ?? TODO add reference here) in LXe based experiment the exact properties of the scintillation and ionization responses to all types of interaction must be well quantified and understood. Mainly, much research has been focused on the scintillation and ionization responses of LXe to events with energy recoil as low as  $\langle O(10 \text{ keV})$  [30–32](TODO add LUX). Specifically the reconstruction of the directionality of recoil nuclei or electrons is of great interest to DM direct detection experiments. Better understanding of these properties may help to reduce background dramatically.

Several existing and proposed experiments such as DRIFT-II [33], DMTPC [34], NEWAGE [35] and MIMAC [36], exploit recoil direction properties. However These experiments are using dilute gas in which the ionization tracks extend to a few millimeters. However, in LXe the track length is estimated to be  $O(100\text{nm})$ . Moreover the topology of the excimers clouds is represented by a complex structure of branches which are formed by secondary recoils [35,50]. These two different properties, track length and structure, makes it highly difficult if not impossible to construct directionality in a LXe experiment. Therefore, a different approach for directionality measurement needs to be adopted for DM LXe based experiments.

The phenomena of an isolated particle in an excited state undergoing a transition to its ground state (i.e. spontaneous decay) as a result of the vacuum electromagnetic field is well described in the theory of quantum electrodynamics. This theory is applicable for an ensemble of particles only when particles interact with the vacuum electromagnetic field separately. In this case the ensemble will emit light an exponential law. The characteristic time,  $\tau_{sp}$ , of a single particle to radiate is equal to the reciprocal of the transition rate  $\Gamma$  from the initially excited level. The radiation pattern in this case is isotropic in its nature, see Fig. 1.5a.

These radiation properties are significantly different when the radiating particles are dense enough. In this case the collective radiation from the ensemble is different than the sum of all particles radiating. This phenomena was first postulated by Dicke [37] in 1954 and was first measured in Xe by Rosenberger in 1965 [38]. In his research the radiation decay time from a two level atomic system was considered and expected to be dependent on the number of radiating particles  $N$ . This type of emission is referred as superradiance. This phenomena

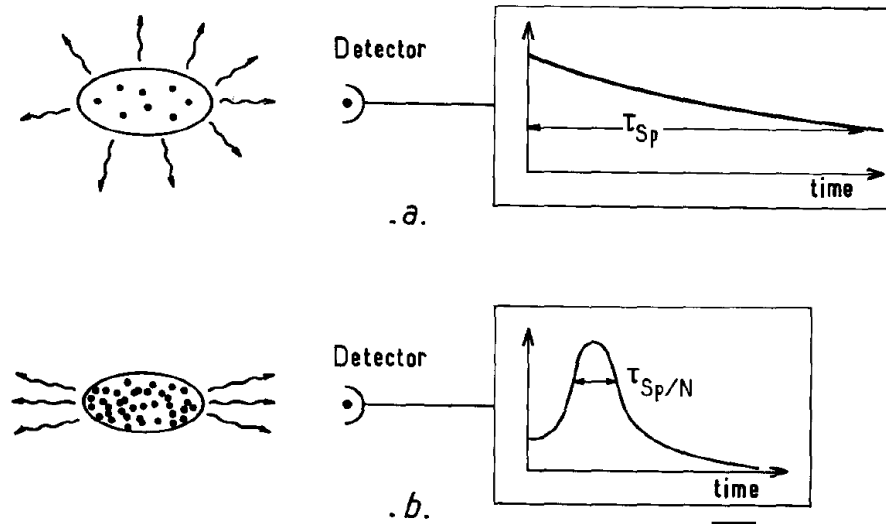


FIGURE 1.5. TODO insert caption here

is due to interaction of the radiating particles with each other via a common electromagnetic radiation field, which results in a correlation between the atomic dipole moment. This correlation leads to a macroscopic optical polarization proportional to  $N$ . Hence the radiation intensity is proportional to  $N^2$ , leading to a pulsed radiation with duration proportional to  $1/N$ , see Fig 1.5b. The phenomena of superradiance has been studied extensively since see [TODO add cite [52, 53]]

An effective self-induction of correlations between dipole moments is a necessary condition for a particles to exhibit a *superradiance*emission. The condition for this to occur are very different then the ones of regular fluorescence. The characteristic time of *superradiance*emission to happen,  $\tau_c \sim 1/N$  must be shorter the relaxation time of the atomic dipole moment,  $\tau_d$ . It also has to be shorter then  $\tau_{sp}$ , however in most cases,  $\tau_d$  is smaller than  $\tau_{sp}$ , hence this is a more stirringit condition. Notice that unlike inverse population that happens in lasers, which occurs due to an external "pump", the correlation build-up between the radiating particles in *superradiance*happens spontaneously in the course of emission process.

The geometry of the radiating particle ensemble influences greatly weather or not a system will exhibit a *superradiance*or standard spontaneous emissions. Specifically the two relevant quantities, are the wavelength  $\lambda$  of the emitted photon, and the size of the radiating particles cloud. A system with linear size much smaller then the emitted photons wavelength.

TODO understand previous paragraph

## 1.4 EFT

The traditional approach for computing predictions of the rate of WIMP-nucleon scattering has been to take only leading-order terms in a WIMP-nucleon effective field theory (EFT) with a very simple treatment of nuclear structure [39]. This leads to two main types of interactions, which are commonly labelled “Spin Independent” (SI) and “Spin Dependent” (SD). However, in recent years many authors have pointed out that in certain theories these interactions may be suppressed or nonexistent, such that otherwise subleading interactions may dominate the scattering process [40]. To account for this possibility in a systematic way, a more sophisticated EFT approach has been developed [41–43]. In the new approach, an effective Lagrangian describing the WIMP-nucleus interaction is constructed, that takes into account all Galilean-invariant operators up to second order in the momentum exchange. This framework introduces new operators associated with different types of nuclear responses, along with the standard SI and SD ones, resulting in a set of fourteen operators  $\mathcal{O}_i$  which may couple independently to protons and neutrons. In Eqs. (1.7) we list these operators following the convention from [42]. The operators depend explicitly on 4 linearly independent quantities:  $\vec{v}^\perp \equiv \vec{v} + \frac{\vec{q}}{2\mu_N}$ , the relative perpendicular velocity between the WIMP and the nucleon,  $\vec{q}$ , the momentum transferred in the scattering event, and  $\vec{S}_\chi, \vec{S}_N$ , the WIMP and nucleon spins.  $\mathcal{O}_2$  is not considered here as it cannot be obtained from a relativistic operator at leading order.

$$\begin{aligned}
\mathcal{O}_1 &= 1_\chi 1_N & \mathcal{O}_9 &= i\vec{S}_\chi \cdot (\vec{S}_N \times \frac{\vec{q}}{m_N}) \\
\mathcal{O}_3 &= i\vec{S}_N \cdot (\frac{\vec{q}}{m_N} \times \vec{v}^\perp) & \mathcal{O}_{10} &= i\vec{S}_N \cdot (\frac{\vec{q}}{m_N}) \\
\mathcal{O}_4 &= \vec{S}_\chi \cdot \vec{S}_N & \mathcal{O}_{11} &= i\vec{S}_\chi \cdot (\frac{\vec{q}}{m_N}) \\
\mathcal{O}_5 &= i\vec{S}_\chi \cdot (\frac{\vec{q}}{m_N} \times \vec{v}^\perp) & \mathcal{O}_{12} &= \vec{S}_\chi \cdot (\vec{S}_N \times \vec{v}^\perp) \\
\mathcal{O}_6 &= (\vec{S}_\chi \cdot \frac{\vec{q}}{m_N})(\vec{S}_N \cdot \frac{\vec{q}}{m_N}) & \mathcal{O}_{13} &= i(\vec{S}_\chi \cdot \vec{v}^\perp)(\vec{S}_N \cdot \frac{\vec{q}}{m_N}) \\
\mathcal{O}_7 &= \vec{S}_N \cdot \vec{v}^\perp & \mathcal{O}_{14} &= i(\vec{S}_\chi \cdot \frac{\vec{q}}{m_N})(\vec{S}_N \cdot \vec{v}^\perp) \\
\mathcal{O}_8 &= \vec{S}_\chi \cdot \vec{v}^\perp & \mathcal{O}_{15} &= -(\vec{S}_\chi \cdot \frac{\vec{q}}{m_N}) \left[ (\vec{S}_N \times \vec{v}^\perp) \cdot \frac{\vec{q}}{m_N} \right]
\end{aligned} \tag{1.7}$$

Unlike the more commonly studied types of interaction (SI,SD), which are not suppressed when  $\vec{q} \rightarrow 0$  and for which the scattering rate on nucleons is expected to be largest for low energy nuclear recoils, some of the new EFT operators depend explicitly on  $\vec{q}$  and so their interaction cross section is suppressed for low momentum transfers. Consequently, their scattering rate peaks at non-zero nuclear recoil energy. For sufficiently high WIMP masses, this may even occur outside typical analysis windows, which usually have an upper range of around 43 keV<sub>nr</sub> (nuclear recoil equivalent energy) since they are designed to search for SI and SD interactions, which

predict exponentially-falling recoil spectra (see Figure ??). Due to the theoretical bias of only considering SI and SD interactions, high energy nuclear recoils remain unexplored in many experiments.

Another typical assumption that can be relaxed is that WIMPs should scatter elastically with nuclei. There exist dark matter models in which the incoming and outgoing WIMPs have different mass states [44] separated by a keV-scale splitting. In the case where the outgoing state is more massive than the incoming state, the cross section for low recoil energies can again be suppressed, this time by scattering kinematics. Recently an inelastic adaptation of the EFT operator framework discussed above was developed [45]. In this case the operators presented in Eqs. 1.7 are modified such that  $\vec{v}_{inelastic}^\perp = \vec{v}_{elastic}^\perp + \frac{\delta_m}{|\vec{q}|^2} \vec{q}$ . We consider this case in section 2.3.2.

CHAPTER



## EFFECTIVE FIELD THEORY SEARCH FOR HIGH ENERGY NUCLEAR RECOILS IN XENON100 DETECTOR

Standard SI,SD analysis concentrate on energy recoils of up to  $O(10)$  keV<sub>nr</sub>, hence a hard high energy threshold of is used for them. In XENON100 this threshold value is 43 keV<sub>nr</sub>. However SI and SD are not the only types of interactions possible. These new interactions which predicts higher recoil energies are considered in the EFT framework (see [1.4](#)). moreover a WIMP may have several mass states, which will also result in a possible higher energy recoil.

The EFT framework of [\[41\]](#) is constructed at the WIMP-nucleon level and so each operator may be present independently for protons and neutrons, though UV models can of course correlate their couplings. The full EFT thus has 28 coupling parameters in addition to the WIMP mass, plus a mass splitting  $\delta$  in the inelastic case. This parameter space is too large to explore in full, so a similar approach to the SI/SD case is taken, assuming only one active operator at a time, considering it equally coupled to protons and neutrons (the “isoscalar” case).

To facilitate the full exploitation of these results by the community, we provide in supplementary material a set of tools for converting any theoretical recoil spectrum  $dR/dE$  into an accurate event rate prediction for this analysis, including all detector response and analysis efficiency effects. This may help to set a mildly conservative but quite accurate limit on arbitrary models in the full EFT parameter space, or any other particle dark matter model for which one can supply the expected recoil spectrum. These tools are described further in Appendix [A](#).

In this work we re-analyze science run II data recorded between February 2011 and March 2012, corresponding to 224.6 live days. The characterization of the detector response to ER interactions is performed using dedicated calibration campaigns with  $^{60}\text{Co}$  and  $^{232}\text{Th}$  radioactive sources, while the response to NR interactions is performed using  $^{241}\text{AmBe}$  neutron source calibration campaigns.

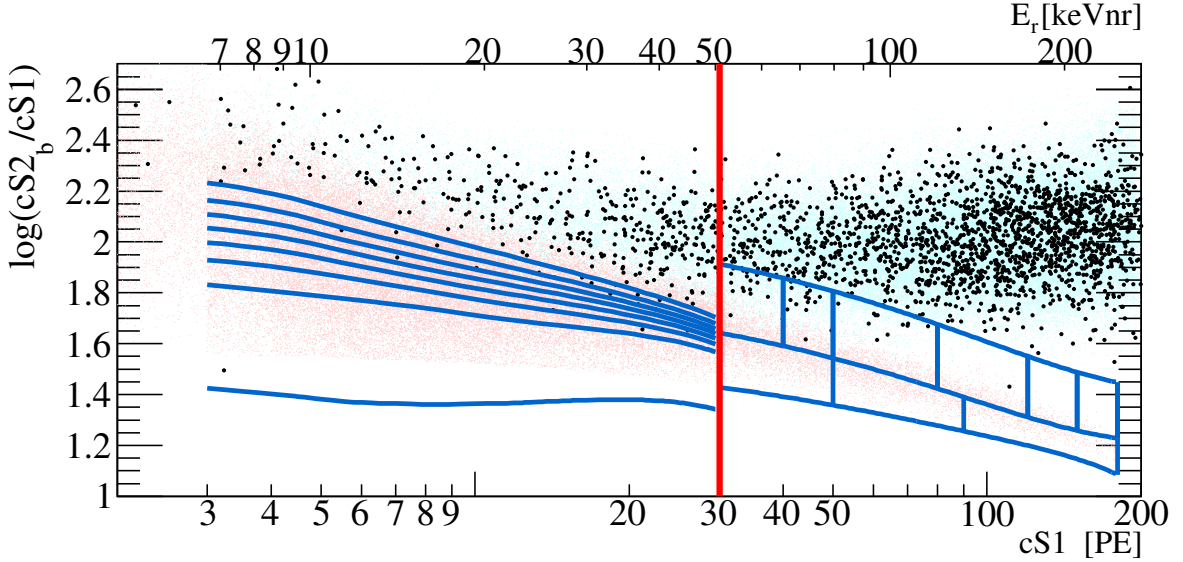


Figure 2.1: Summary of regions of interest, backgrounds, and observed data. ER calibration data, namely  $^{60}\text{Co}$  and  $^{232}\text{Th}$  data is shown as light cyan dots. NR calibration data ( $^{241}\text{AmBe}$ ) is shown as light red dots. Dark matter search data is shown as black dots. The red line is the threshold between the low and high energy channels. The lines in blue are the bands. For the low-energy channel the bands are constructed to achieve constant expected signal density, and are operator and mass dependent, shown here for a  $50 \text{ GeV}/c^2$  WIMP using the  $\mathcal{O}_1$  operator. For the high-energy region, the nine analysis bins are presented also in blue lines.

This work extends the previous results [5, 46], referred to in the following as the low-energy channel, with a new study exploring the recoil energy range between  $(43 - 240) \text{ keV}_{\text{nr}}$ . The data analysis is divided into two mutually exclusive channels, one optimized for low energies and ranging from  $(3-30) \text{ PE}$  in  $\text{cS1}$  (low-energy), the other optimized for high energies recoils ranging from  $(30-180) \text{ PE}$  in  $\text{cS1}$  (high-energy). These two analyses are then combined statistically.

## 2.1 Low energy channel

This analysis channel relies on the re-analysis of run II data described in [5]. The region of interest (ROI), the background expectation models, data selections and their acceptances are mostly unchanged and so are only briefly summarized here. Differences with respect to said results are highlighted when present.

The ROI for this channel is defined in the  $(y, \text{cS1})$ -plane and is shown in Figure 2.1. The lower bound on  $y$  corresponds to a  $3\sigma$  acceptance quantile (as a function of  $\text{cS1}$ ) of a  $20 \text{ GeV}$  WIMP mass signal model assuming an  $\mathcal{O}_1$  (SI) interaction, while the upper bound is fixed at  $y = 2.7$ . The range in  $\text{cS1}$  is selected as  $(3 - 30) \text{ PE}$ . The ROI is further divided into eight sub-regions (also called bands) depending on the operator  $\mathcal{O}_i$  and on the WIMP mass hypothesis. These bands are arranged to achieve constant expected signal density in each region, as described in [5].

Other than falling into the ROI, an event should fulfill several additional selection criteria (cuts). Data quality and selection cuts are defined to remove events with poor data quality or noisy signals. Events are discarded if they present a time-coincident signal in the outer LXe veto, S2 signals below threshold, multiple-scatters, or are localized outside a predefined fiducial volume of 34 kg. In addition, this analysis channel uses the post-unblinding cuts and data reprocessing described in [5]. More details on these selection criteria and their relative WIMP signals acceptances can be found in [5, 47].

Note that this analysis channel does not employ a variable lower S1 threshold as a function of the event position in the TPC, but instead applies a fixed lower threshold cut on cS1 at 3 PE, conversely to the choice made in [5].

The expected background is modeled separately for ER and NR contributions which are then scaled to exposure and added together. The NR background is estimated by Monte Carlo simulation and accounts for the radiogenic and cosmogenic neutron contributions [48]. The ER background is parametrized as the linear combination of Gaussian-shaped and non-Gaussian components. The former is obtained via a parametric fit of the  $^{60}\text{Co}$  and  $^{232}\text{Th}$  calibration data, as discussed in [46].

The latter, which consist of anomalous events such as those presenting incomplete charge collection or accidental coincidence of uncorrelated S1s and S2s, is evaluated via dedicated techniques described in [5].

Systematic uncertainties on the background model arising from the Gaussian parametrized fit, and from the normalisations of the NR and non-Gaussian components, have been evaluated and propagated to each band. These errors are small with respect to the statistical uncertainties of each band, which are conservatively taken as the overall uncertainty [5], as discussed in Sec. 2.4.

## 2.2 High energy channel

This analysis channel targets high energy nuclear recoils and is the focus of this work. The data selection criteria used are based on the criteria described in detail in [47], which were optimized for high acceptance to low energy nuclear recoils. Most of these cuts were found to be fully compatible with (or easily extended) to high energy depositions, however some required more comprehensive studies, which are described in the following .

The width of an S2 pulse increases with the depth ( $z$ ) of the interaction. This is due to the diffusion of the electron cloud during its propagation through the liquid xenon. Since low energy S2 events show larger spread due to low statistics of drifted electrons, the cut was previously defined in an energy-dependent way. However, for the large recoil energies considered in this channel, this energy dependency is no longer valid. We therefore use here a cut on the S2 width which is a function of the depth of the interaction alone.

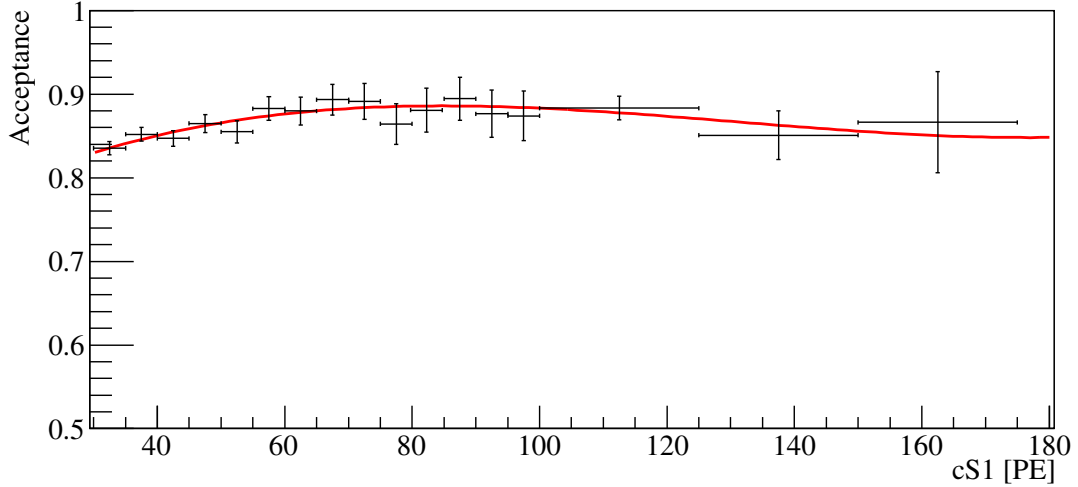


Figure 2.2: The total acceptance of all cuts used. Data from calibration is shown in black, with a 3rd order polynomial fit in red.

As a WIMP will interact only once in the detector, we remove events which have more than one S2. We adopt in this analysis a cut that is more suitable to higher energies and demand a single S2 in a  $160\ \mu\text{s}$  window, instead of a linear dependence between the second S2 size and the first.

To define the interaction's exact location in  $(x, y)$ , we use several algorithms, one of which is based on a Neural Network (NN) [47]. The NN was not trained to recognize high energy ER events and therefore a cut on the NN reconstruction quality is not suitable for this analysis. We therefore discard this cut but keep all other selections on position reconstruction quality, which is sufficient to ensure a correct position reconstruction.

The total acceptance to WIMP signals is computed based on  $^{241}\text{AmBe}$  calibration data as a function of cS1, following the procedure described in [47]. We present this function in Figure 2.2, where the total acceptance is fitted using a third order polynomial.

We define our signal region in the discrimination  $(y, \text{cS1})$ -plane using  $^{241}\text{AmBe}$  calibration data. The region of interest is shown in Figure 2.1 as blue contour lines. The upper bound in  $y$  is defined such that the contribution due to xenon inelastic interaction lines is negligible. The lower bound is defined as the  $3\sigma$  acceptance quantile of the  $^{241}\text{AmBe}$  distribution.

We divide our signal region into two bands in  $y$ , constructed such that the  $^{241}\text{AmBe}$  data sample is equally distributed in between them. The number of events in each band is  $\sim 3000$ . The bands are further divided into nine bins, the number and boundaries of which have been optimized via Monte-Carlo (MC) simulation. The definitions of the bins boundaries are presented in Table 2.1 and in Figure 2.1.

The main source of background results from ER leakage. We therefore estimate the background distribution in the ROI using  $^{60}\text{Co}$  and  $^{232}\text{Th}$  calibration events. Contributions from

#	Band	Energy Range (cS1)	# Background Events	# Data Events
1	upper	30 - 40	24±5	20
2	upper	40 - 50	16±3	17
3	upper	50 - 80	12±3	11
4	upper	80 - 120	1.1±0.3	1
5	upper	120 - 150	(1.0±0.5)×10 <sup>-1</sup>	1
6	upper	150 - 180	(0.8±0.4)×10 <sup>-1</sup>	0
7	lower	30 - 50	0.9±0.3	0
8	lower	50 - 90	(3.5±1.2)×10 <sup>-1</sup>	0
9	lower	90 - 180	(1.8±0.7)×10 <sup>-1</sup>	0

Table 2.1: Definitions and contents of the analysis bins for the high energy channel. The expected background counts are calculated by taking the calibration sample and scaling it by  $6.54 \times 10^{-3}$ , which is the ratio of observed counts to calibration counts in a sideband.

radiogenic and cosmogenic neutrons, as well as accidental coincidence, are negligible for such a high energy recoil. In Table 2.1 we report the background expectation in the ROI along with the observed events for each bin. Here the background expectation is computed by scaling the calibration sample yield by  $6.54 \times 10^{-3}$ , which is the ratio of observed counts to calibration counts in an independent sideband. The sideband is defined above the upper limit of this analysis and below the ER calibration band mean. Note that in the computation of exclusion limits, the background normalization is fitted to data, rather than using the sideband normalization, as described in section 2.4.

## 2.3 Signal model

The signal model is produced by taking a theoretical event rate spectrum, the production of which is described in sections 2.3.1 and 2.3.2, and applying the analysis acceptance and detector response as described in [47] to obtain the expected event rate in the detector in terms of detector variables (i.e. cS1, cS2<sub>b</sub>). In both analysis channels, we use Eq. 2.1 in order to compute the expected average cS1 for a given NR energy,

$$(2.1) \quad \langle cS1 \rangle = E_{nr} \cdot (L_y \mathcal{L}_{eff}) \cdot \left( \frac{S_{nr}}{S_{ee}} \right)$$

where  $E_{nr}$  is the recoil energy,  $L_y$  is the average light yield in the detector,  $\mathcal{L}_{eff}$  is the scintillation efficiency relative to 122keV<sub>ee</sub> as a function of  $E_{nr}$ , and  $S_{ee}$  and  $S_{nr}$  are the quenching factors due to the externally applied electric field. Aside from  $E_{nr}$  and  $\mathcal{L}_{eff}$  these parameters have fixed values, namely  $L_y = 2.28 \pm 0.04$ ,  $S_{nr} = 0.95$ , and  $S_{ee} = 0.58$ . Recoils below 3 keV<sub>nr</sub> are assumed to produce no light. For details of the physics behind these parameters and the construction of the signal probability density function (PDF) please see [5, 47].

For the low-energy region, the expected cS2<sub>b</sub> signal is computed following [49] using Eq. 2.2,

$$(2.2) \quad \langle cS2_b \rangle = E_{nr} \mathcal{Q}_y Y$$

where  $Y = 8.3 \pm 0.3$  is the amplification factor determined from the detector response to single electrons [50], and  $\mathcal{Q}_y$  is the charge yield as a function of  $E_{nr}$ . Applying the detector and PMT responses, and the acceptance as in [5], defines the low-energy signal model over the region 3 PE < cS1 < 30 PE, with cS2<sub>b</sub> > 73.5 PE as the S2 threshold.

Eq. 2.2 hides a subtlety. The actual cS2<sub>b</sub> PDF is composed of two pieces, a Poisson term associated with the initial charge liberation and a Gaussian term associated with the PMT response and other detector effects:

$$(2.3) \quad p_{S2}(cS2_b | E) = \sum_{N'} P_{pmt}(cS2_b | YN', \sigma_Y \sqrt{N'}) \cdot \text{Pois}(N' | \mu_Q)$$

where  $\mu_Q = E_{nr} \mathcal{Q}_y$  is the expected number of liberated charges in a nuclear recoil event of energy  $E$ , and  $N'$  is the actual number of liberated charges. The amplification factor  $Y$  is applied to the actual number of liberated charges  $N'$ , not the expected number  $\mu_Q$ . Associated with this is the variance of the Gaussian response PDF,  $\sigma_Y \sqrt{N'}$ , where in this analysis  $\sigma_Y = 6.93$  as measured and described in [50].

For the high energy region we cannot produce the S2 distribution in the same way as the method in [49], since it has not been calibrated for such high recoil energies. We therefore use the NR calibration data distribution in  $\log(cS2_b/cS1)$  to estimate the WIMP distribution. Above 180 PE in cS1, the event yield of <sup>241</sup>AmBe data is too low to estimate the distribution accurately. This forms the upper bound of this analysis. With the cS2<sub>b</sub> distribution determined by this empirical method, we require only a prediction of the cS1 distribution. This is obtained from Equation (2.1), followed by the application of detector and PMT responses, as well as the acceptance given in Figure 2.2, which completes the high-energy signal model definition.

Figures 2.3 and 2.4 show signal distribution examples for two EFT operators and for the low and the high energy region, respectively. In both cases, the signal distributions are normalized to yield 5 events in the total energy range (low-energy and high-energy).

### 2.3.1 Elastic scattering

The expected recoil energy spectrum of each WIMP mass for each EFT operator is calculated using the Mathematica package DMFormFactor supplied by Anand et. al. [42, 43]. We use standard assumptions as in previous analyses (e.g [5]) regarding the local dark matter density and velocity distribution, namely  $\rho_{\text{local}} = 0.3 \text{ GeV}\cdot\text{cm}^{-3}$  and a Maxwell-Boltzman distribution with a mean given by the local circular velocity  $v_0 = 220 \text{ km/s}$  and cut off at an escape velocity of  $v_{\text{esc}} = 544 \text{ km/s}$ . The responses of xenon nuclei to a scattering event are computed from one-body density matrices provided with the package, in contrast to the Helm form factors which have been used

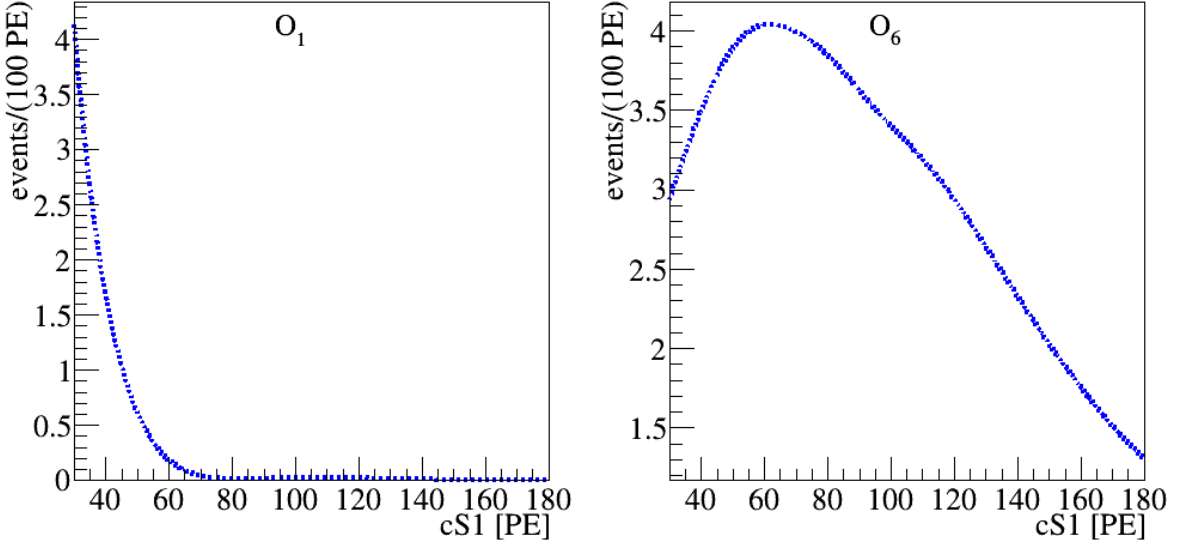


Figure 2.3: The expected signal in the high energy region for a  $300 \text{ GeV}/c^2$  WIMP mass, normalized to 5 events. Left(right) is the spectra for  $\mathcal{O}_1(\mathcal{O}_6)$ . Notice that for  $\mathcal{O}_1$  most of the events are not expected to deposit energy higher than 30 PE whereas for  $\mathcal{O}_6$  a large fraction of the events appear in this region.

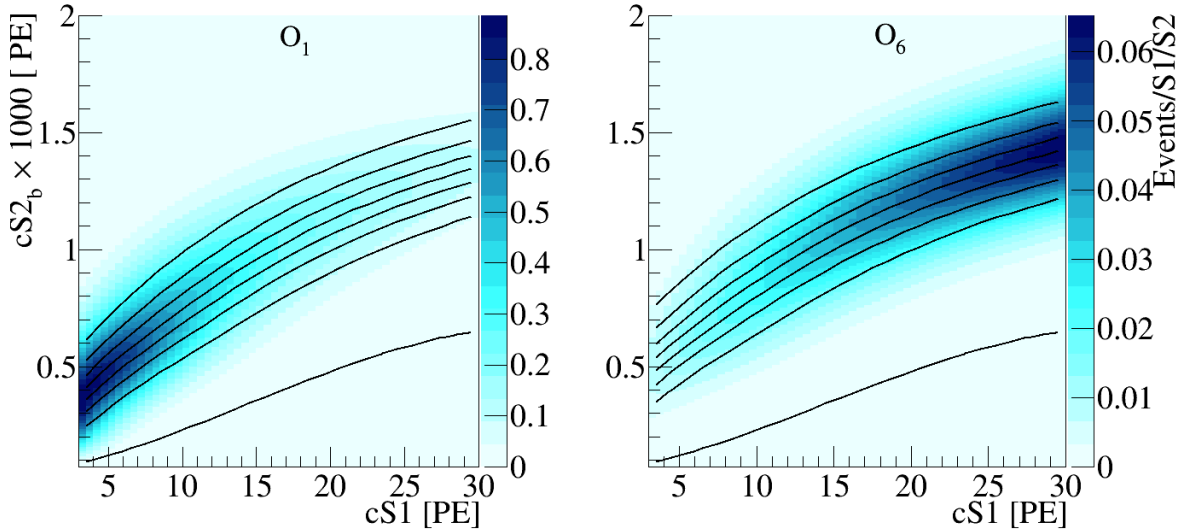


Figure 2.4: The expected signal in the low energy region for a  $300 \text{ GeV}/c^2$  WIMP mass, normalized to 5 events. Left(right) is the spectra for  $\mathcal{O}_1(\mathcal{O}_6)$ . Notice that for  $\mathcal{O}_1$  most of the events are expected to deposit energy lower than 30 PE whereas for  $\mathcal{O}_6$  a large fraction of the events do not appear in this region at all. The black lines indicate the bands constructed on these specific mass and operator models, and are dividing the signal into 8 equally distributed signal sub-regions. This parameter space can be mapped with a one to one mapping to the  $(y - cS1)$  space.

in previous analyses. These spectra are produced for the seven most abundant xenon isotopes (128, 129, 130, 131, 132, 134 and 136), combined in proportion to the abundance of these isotopes in the XENON detector [51], then translated into expected signal rates via the method described above.

### 2.3.2 Inelastic WIMP scattering

To obtain recoil spectra for WIMP-nucleon scattering for all EFT operators with inelastic kinematics, we use a modified version of DMFormFactor provided by Barell et. al. [45]. The authors have modified the original package to enforce the new energy conservation condition  $\delta_m + \vec{v} \cdot \vec{q} + |\vec{q}|^2/2\mu_N = 0$ , primarily by replacing  $\vec{v}_{\text{elastic}}^\perp \rightarrow \vec{v}_{\text{inelastic}}^\perp = \vec{v}_{\text{elastic}}^\perp + \frac{\delta_m}{|\vec{q}|^2} \vec{q}$  in the definitions of the EFT and nuclear operators, giving rise to the well-known minimum velocity for scattering

$$(2.4) \quad v_{\min}/c = \frac{1}{\sqrt{2m_N E_R}} \left| \frac{m_N E_R}{\mu_N} + \delta_m \right|$$

where  $\mu_N$  is the WIMP-nucleon reduced mass.

Assumptions regarding the dark matter halo and nuclear physics are unchanged. The mass splitting  $\delta_m$  between dark matter states is varied from (0 – 300) keV, safely beyond the value at which the predicted rate is zero for the entire mass range we consider.

## 2.4 Statistical inference

The statistical interpretation of data is performed using a binned profile likelihood method, in which hypothesis testing relies upon a likelihood ratio test statistic,  $\tilde{q}$ , and its asymptotic distributions [52] to constrain the coupling constants  $c_k$  for each operator  $\mathcal{O}_k$ . The two analysis channels are combined by multiplying their likelihoods together to produce a joint likelihood function.

$$(2.5) \quad \mathcal{L} = \mathcal{L}_{\text{lowE}(c_i^2, \mathcal{Q}_y, \mathcal{L}_{\text{eff}})} \times \mathcal{L}_{\text{highE}(c_i^2, \mathcal{L}_{\text{eff}})}.$$

Both analyses parametrize the NR relative scintillation efficiency,  $\mathcal{L}_{\text{eff}}$ , based on existing measurements [53]. Its uncertainty is the major contributor to energy scale uncertainties and is considered as correlated between the two analysis channels via a joint nuisance likelihood term. Throughout this study, all the parameters related to systematic uncertainties are assumed to be normally distributed.

For the low energy channel an extended likelihood function is employed which is very similar to the one reported in [54] and described in detail in [5]. The  $(y, cS1)$ -plane is divided into eight WIMP mass dependent bands where events are counted. This binned approach is extended with

the corresponding cS1-projected PDF of each band. The total normalization of the background is fit to data, and an uncertainty is assigned to the relative normalization of each band according to the corresponding statistical uncertainty of the calibration sample.

Signal shape variations due to energy scale uncertainty are modeled via simulation. These include the said  $\mathcal{L}_{\text{eff}}$  uncertainties and additionally the charge yield uncertainties, which are parametrized based on  $\mathcal{Q}_y$  measurement as described in [49].

The low energy likelihood function is shown in Eq. ??,

$$(2.6) \quad \mathcal{L}_{\text{lowE}} = \mathcal{L}_1(c_k^2, \mathcal{L}_{\text{eff}}, \mathcal{Q}_y) \mathcal{L}_2(\epsilon_b) \mathcal{L}_3(\mathcal{L}_{\text{eff}}, \mathcal{Q}_y).$$

$$(2.7) \quad \begin{aligned} \mathcal{L}_1(c_k^2, \mathcal{L}_{\text{eff}}, \mathcal{Q}_y) &= \prod_j \text{Poiss}(n^j | \epsilon_s^j M_s(c_k^2) + \epsilon_b^j M_b) \times \\ &\prod_{i=1}^{n^{i,j}} \frac{\epsilon_s^j M_s(c_k^2) f_s^j(cS1^i) + \epsilon_b^j M_b f_b^j(cS1^i)}{\epsilon_s^j M_s + \epsilon_b^j M_b}, \end{aligned}$$

where  $f_s^j$  and  $f_b^j$  are the probability density functions of the signal and background respectively in band  $j$ . and  $M_s$  and  $M_b$  are the maximum likelihood estimators for the total number of signal and background events respectively.

$$(2.8) \quad \mathcal{L}_2 = \prod_j \text{Poiss}(n_b^j | \epsilon_b^j N_b)$$

The high energy channel analysis employs a binned likelihood function. Observed and expected event yield are compared in the nine ROI ( $y$ , cS1)-bins described in section 2.2. Given the large statistical uncertainty of the background model the above extended likelihood approach is not repeated here. Instead, the maximum likelihood estimation of the background expectation in each bin is constrained by the statistical uncertainty of the calibration sample, while the total normalization is fit to the data. Additionally, to account for potential mis-modeling of the expected background distribution, mainly due to anomalous multiple scatter events, a systematic uncertainty of 20% is assigned independently to each bin. In the high energy channel, uncertainty on the signal acceptance of analysis selections are computed for each signal hypothesis using the parametrized acceptance curve shown in Figure 2.2. Uncertainties on the signal model ( $y$ , cS1) distribution due to  $^{241}\text{AmBe}$  sample statistical fluctuations, as well as energy scale shape variation due to  $\mathcal{L}_{\text{eff}}$  uncertainties, are taken into account.

The high energy likelihood function is defined in Eq. 2.9

$$(2.9) \quad \mathcal{L}_{\text{highE}}(c_k^2, \mathcal{L}_{\text{eff}}) = \prod_i \left( \text{Poiss}(n_i^{obs} | n_i^s + n_i^b) \times \text{Gauss}(\eta_i^b) \right) \times \mathcal{L}_{\text{stat}}(\epsilon_j^s, \epsilon_i^b) \times \mathcal{L}_{\text{unc}}^s(\mathcal{L}_{\text{eff}}, A)$$

where the product goes over all 9 bins,  $\epsilon_i^b$  is the fraction of background event in **bin**  $i$  and  $\epsilon_j^s$  is the fraction of AmBe data in **band**  $j$ . This means the uncertainty on the signal is assessed per band.  $n_i^s = N_{\text{tot}}^s(c_k^2, \mathcal{L}_{\text{eff}}) \times \zeta_{i,j}^s(\mathcal{L}_{\text{eff}}, \epsilon_j^s)$  is the number of signal events in bin  $i$ ,  $\zeta_{i,j}^s(\mathcal{L}_{\text{eff}}, \epsilon_j^s)$  is the fraction of signal events in bin  $i$  which is in band  $j$ .  $n_i^b = N_{\text{tot}}^{\text{cal}} \times \tau \times \epsilon_i^b(\eta_i^b)$  is the number of background events in bin  $i$ .  $\tau$  is the overall normalization of background to data, and is a free parameter.

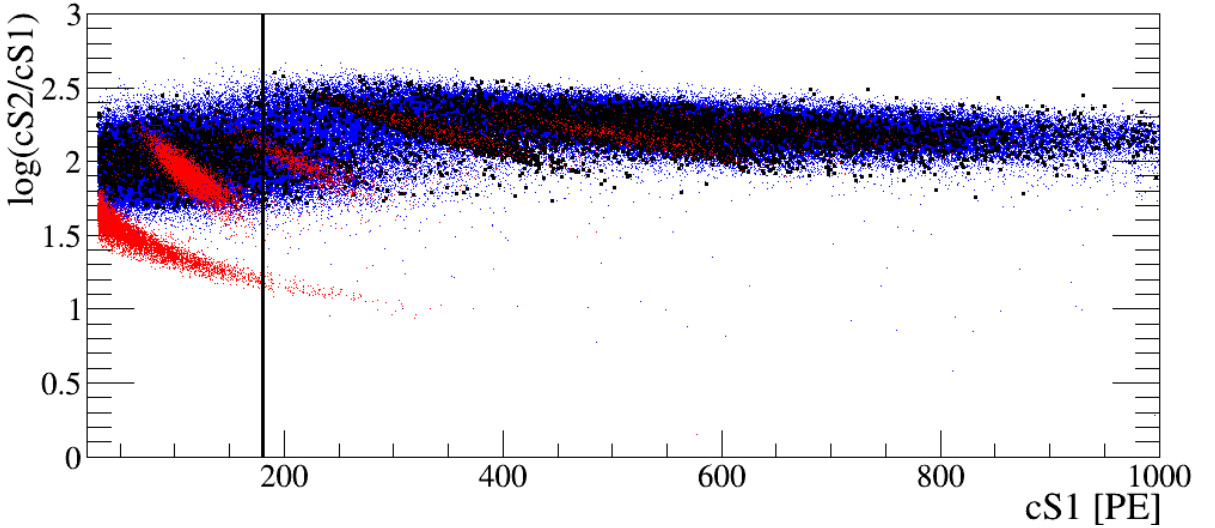


Figure 2.5: The full XENON100 dark matter science run data up to 1000 PE in cS1 (shown in black). In blue we show data from ER calibration ( $^{60}\text{Co}$  and  $^{232}\text{Th}$ ) and in red from NR calibration ( $^{241}\text{AmBe}$ ). See text for details on these populations. While the black vertical line represents the highest energy considered for quantitative interpretation in this analysis, there is no indication of elastic NRs even above that energy.

## 2.5 Data From Recoil Energies Up To 1000 PE

Upon completing our analysis, we examined data in the cS1 region above 180 PE, up to 1000 PE, since it will not be analyzed in any future XENON publications. We used the same data selection criteria as those applied for the high-energy channel. These selection criteria are not optimized for the new even-higher energies and may exhibit a drop in acceptance for NRs to below 50%. Due to the lack of NR calibration data and of a rigorous background model in this energy range, a quantitative and statistically solid inference on dark matter hypotheses is impractical. Nonetheless, we provide a plot of the data here. Figure 2.5 shows the distribution of science data in this extended range (in black) together with NR (in red) and ER calibration data (in blue).

The NR calibration data shows the NR band from elastic scattering, with the aforementioned loss of statistics at energies above 180 PE clearly visible. Also visible are lines in the ER band from the inelastic scattering of neutrons on  $^{129}\text{Xe}$  (39.6 keV at 130 PE) and  $^{131}\text{Xe}$  (80.2 keV at 220 PE) as well as the delayed de-excitation of  $^{131m}\text{Xe}$  (169.3 keV at 350 PE) and  $^{129m}\text{Xe}$  (236.1 keV at 500 PE). ER calibration data is shown in blue and indicates the distribution of the prevalent background in this energy range. Since the detector is optimized for low-energy events, large S2 pulses saturate the PMT bases. This is visible in the ER band above 250 PE.

Finally, data from the dark matter search is shown in black. As can be seen, there is no indication of elastic NRs at energies above those analyzed in this study.

## 2.6 Results

A benchmark region of interest is defined between the upper and lower thresholds in cS1 for each channel. This region is bounded in  $y$ -space from above by the  $^{241}\text{AmBe}$  NR mean line and below by the lower  $3\sigma$  quantile of the  $^{241}\text{AmBe}$  neutron calibration data. The expected background in the region is  $3.0 \pm 0.5_{\text{stat}}$  (low-energy) and  $1.4 \pm 0.3_{\text{stat}}$  (high-energy). The number of DM candidates in this benchmark region is 3 (low-energy), and 0 (high-energy). Consequently, the data is compatible with the background-only hypothesis and no excess is found.

For the elastic scattering case, a 90%  $\text{CL}_S$  [55] confidence level limit is set on the effective coupling constant,  $c_i$ , for all operators and masses in the range of  $10 \text{ GeV}/c^2$  to  $1 \text{ TeV}/c^2$ . The  $c_i$  are dimensionful, with units of  $[\text{mass}]^{-2}$ , so we first convert them to dimensionless quantities by multiplying them by  $m_{\text{weak}}^2 = (246.2 \text{ GeV})^2$ , following the conventions of [42].

These limits are shown in Fig. 2.6 in black, along with limits from CDMS-II Si, CDMS-II Ge and SuperCDMS [1].

For the inelastic scattering case, 90%  $\text{CL}_S$  confidence level limits on the coupling constants (again scaled by  $m_{\text{weak}}^2$ ) are set. Fig. 2.7 shows limits on the  $\mathcal{O}_1$  (SI) coupling constant as a function of mass splitting and WIMP mass, Fig. 2.8 shows limits for all other operators as a function of the mass splitting  $\delta_m$  with a fixed WIMP mass of  $1 \text{ TeV}/c^2$ , projections of results from CDMS-II [56], ZEPLIN-III [57], and XENON100 [58] in the coupling constant and  $\delta_m$  parameter space are also reported.

For the elastic operator  $O_1$  our results can be compared to those of standard SI analyses by computing the relevant zero-momentum WIMP-nucleon cross-sections. This is not simple to do rigorously because the treatment of nuclear structure used in our analysis is different than in standard analyses, however this difference is small for scattering via  $O_1$ . We can therefore quite safely use the ‘traditional’ correspondence [59]

$$(2.10) \quad \sigma_N^{\text{SI}} = \left( C_1^N \right)^2 \frac{\mu_{\chi,N}^2}{\pi}$$

where  $\mu_{\chi,N}$  is the WIMP-nucleon reduced mass. Standard SI analyses assume isospin-conserving interactions, as we do in this analysis, so we can simply set  $C_1^N = C_1^0$ , such that  $\sigma_p^{\text{SI}} = \sigma_n^{\text{SI}}$ .

In principle a similar comparison can be done between our limit on the  $O_4$  coupling and standard SD analysis limits, however this time the standard analyses do *not* assume isospin-conserving interactions. Instead they typically assume maximal isospin violation, that is, assuming that WIMPs couple either protons or neutrons. Limits are then derived independently on  $\sigma_p^{\text{SD}}$  and  $\sigma_n^{\text{SD}}$ . Because of this difference in assumptions, our limits on SD couplings are not directly comparable to usual analyses. However, they can be recast under the appropriate alternate model assumptions using the detector response tables we provide in the supplementary material.

CHAPTER 2. EFFECTIVE FIELD THEORY SEARCH FOR HIGH ENERGY NUCLEAR RECOILS IN XENON100 DETECTOR

---

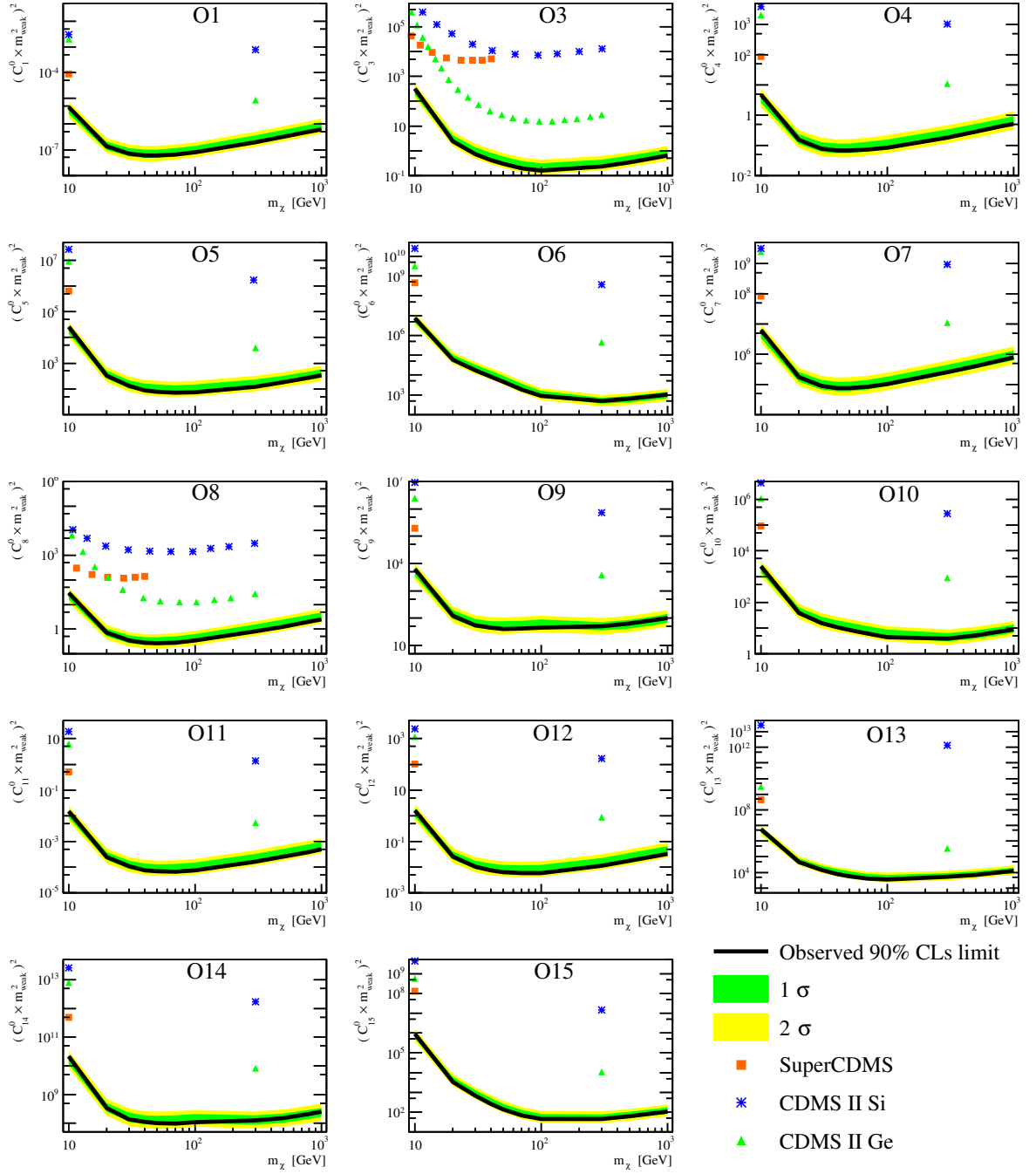


Figure 2.6: The XENON100 limits (90% CL<sub>S</sub>) on isoscalar dimensionless coupling for all elastic scattering EFT operators. The limits are indicated in solid black. The expected sensitivity is shown in green and yellow(1 $\sigma$  and 2 $\sigma$  respectively). Limits from CDMS-II Si, CDMS-II Ge, and SuperCDMS [1] are presented as blue asterisks, green triangles, and orange rectangles, respectively. For operator 3 and 8 a full limit was published, for all other operators only  $m_\chi = 10$  and  $m_\chi = 300$  are available.

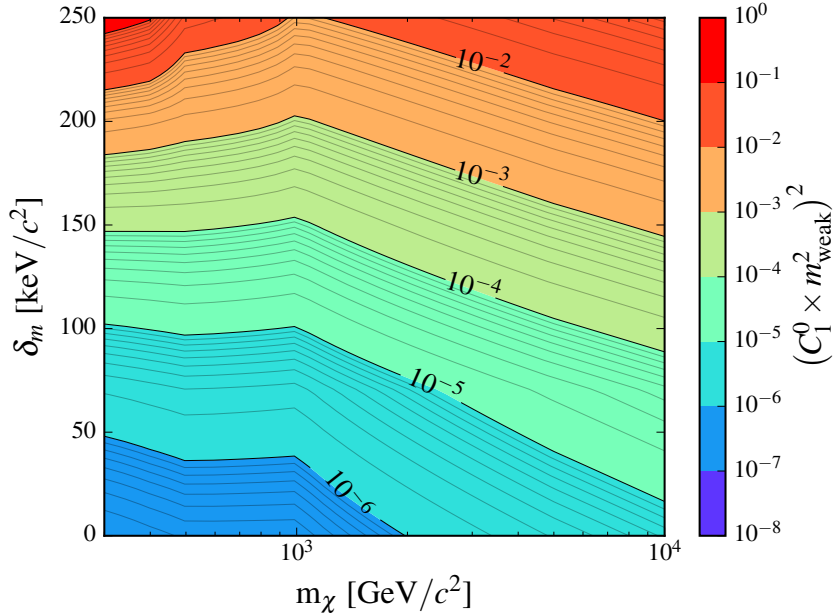


Figure 2.7: 90% CL<sub>S</sub> limits, for the inelastic model, on the magnitude of the coupling constant for  $\mathcal{O}_1$ , reported as a function of the WIMP mass and mass splitting  $\delta$ .

## 2.7 Summary

In this section I have shown the an analysis of XENON100 data at recoil energies above 43 keVnr, with the new high energy bound set to 240 keVnr. I considered in this analysis two models which predict interactions in this energy region: an EFT approach for elastic WIMP-nucleon scattering, and a similar EFT approach but considering instead inelastic WIMP-nucleon scattering. The observed data was compatible with background expectations, and 90% CLS exclusion limits were constructed for WIMP masses between (10-1000) GeV.

CHAPTER 2. EFFECTIVE FIELD THEORY SEARCH FOR HIGH ENERGY NUCLEAR RECOILS IN XENON100 DETECTOR

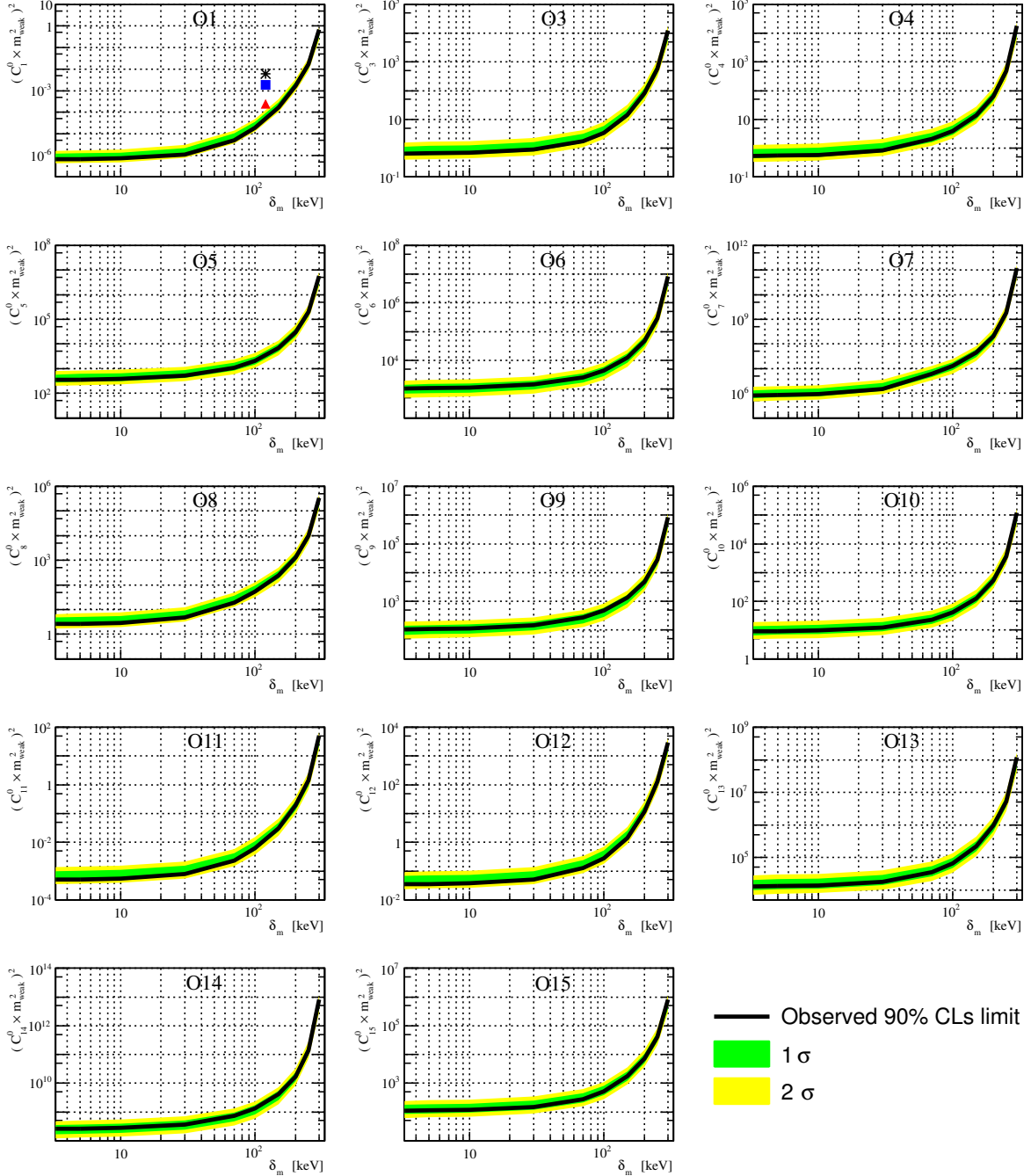


Figure 2.8: The XENON100 90% CL<sub>S</sub> limits on a 1 TeV/c<sup>2</sup> WIMP isoscalar dimensionless coupling constant as function of the WIMP mass splitting  $\delta_m$  for all inelastic scattering EFT operators. Limits are indicated in solid black. The expected sensitivity is shown in green and yellow ( $1\sigma$  and  $2\sigma$  respectively). For  $\mathcal{O}_1$  (SI) results from XENON100(red triangle) CDMS-II(blue rectangle) and ZEPLIN-III(black star) are overlaid.

CHAPTER



## DIREXENO

In Liquid Xenon experiments, the cloud of excimers produced when a particle recoils energy in xenon is estimated to have a complex shape. Nonetheless it is expected to have a typical size of  $O(100\text{nm})$ . Hence it is expected that the excimer cloud might undergo a *superradiance* emission. A variation in the temporal time of radiation between ERs and NRs might exist due to the size of the excimer cloud. This can improve the discrimination between background(ER) and signal(NR) for LXe DM detectors. Moreover whether the emitted radiation is correlated to the incoming exciting particle momentum, can be a more powerful tool for background reduction. Discarding events coming from the direction of the sun for example, is necessary once the neutrino floor(TODO add cite neutrino floor) will be crossed.

Early studies conducted by Basov [60] (experimentally) and in NIST(TODO add cite NIST) (theoretically) both present the option of generating a coherent radiation in the VUV regime ( 178nm). The experimental setup was designed to bombard the LXe with 800 keV electron current pulse exciting (10 ns) the LXe. The constant electron current causes a reverse population constantly. In contrary in direct detection of DM experiments, there is no "pump" producing this inverse population. The study of whether a cloud of excimers caused by a single interaction can exhibit *superradiance* is still absence.

In this chapter we discuss Direxeno (Directional Xenon). An experimental setup designed at measuring *superradiance* or any other non-linear effect in LXe.



## CALIBRATION SYSTEM FOR XENON1T

One of the most important prerequisite for having a successful detector is a good understanding of the response for different types of interactions. In "low-background" experiments the usual technique for quantifying the detector response for different radiation types, is by creating a controlled data sample for each type of interaction. This sample is obtained by exposing the detector to a radioactive source with intensity which is order of magnitude greater than the background rate. This insures that the events in the detector are coming from a specific type of interaction, with a well defined energy. The study of these induced signals is known as "*detector calibration*"

The two measurable of XENON100 and XENON1T are the prompt scintillation (S1) and the proportional scintillation (S2). The efficiency of detecting the scintillation light determines the energy threshold of the detector. Both light and charge yields can be attenuated by impurities in the LXe.

The non uniformity of scintillation light collection signal s due to solid angle effects, Rayleigh scattering length, reflectivity, transmission of the electrodes, etc. lead to a position-dependent S1 signal. Extracted electrons are absorbed by impurities, mainly by oxygen and water, the number of electrons reaching the GXe is depth (z) dependent. Hence a correction to the energy scale both in S1 and S2 should be applied. This calibration is known as light and charge collection.

Most of the background of XENON1T is due to electromagnetic interactions, predominantly,  $\gamma$ s, interacting in the target. Most of the background events occur near the TPC walls, this is due to the stopping power of LXe. Therefore, most of the background rejection is achieved through fiducialization, namely limiting the science data to a smaller FV volume. In addition to that the ratio between S2 and S1 for NRs (expected signal) and ERs (background) is different in nature. The main discrimination power of XENON1T is via this ratio. A good understanding

of the different response to the two interaction types is important to quantify the background leakage distribution. Also the response for NR is important to produce data-MC matching. This is, amongst other, important to understand the acceptance of the different data selection criteria applied in the analysis process. This calibration is known as "NR and ER bands"

The trivial and easiest approach to calibrate the detector is the one applied in XENON100. Simply place a gamma source outside the detector and create the controlled data sample. However, this approach is not applicable for XENON1T due to various reasons. The main obstacle is to deploy the source inside the water tank. Moreover, for each calibration type, events need to fulfill certain data selection criteria which dictates the rate and energies needed.

For the light and charge collection calibration the full absorption peak is used; therefore even low-energetic sources, such as  $^{137}\text{Cs}$  (662 keV  $\gamma$ s) can be used to produce a fairly large data sample in a reasonable time. For the ER band calibration, just placing a source near the detector is not sufficient. There are more data selection criteria needed for this calibration.

A good ER band calibration event should have low energy deposition ( $2 - 15\text{keV}_{\text{ee}}$ ), should scatter only once in the detector, should occur inside the FV and should scatter only once in the detector. Notice that the diameter of XENON1T TPC is  $\sim 1$  meter meaning a  $\gamma$  needs to penetrate the FV (travel  $\sim 10$  cm inside LXe) scatter in a small angle and travel outside of the TPC ( $\sim 90$  cm) without scattering again in order to produce a good calibration event. The probability for that to happen, even for a 2 MeV source is very low  $\sim 10^{-7}$ . Because the detector cannot process data at high rates, the amount of time needed for this calibration is extremely long, and a new approach is needed.

Internal calibration techniques, in which a short lived radioactive source is dissolved inside the LXe is one of the calibration methods used in XENON1T. The radioactive sources used are:  $^{83m}\text{Kr}$ , tritiated methane  $\text{CH}_3\text{T}$  and  $^{220}\text{Rn}$ .

In this section I describe the new technique for external calibration, mainly ER band calibration, including the radioactive sources used, the holders of the sources which will confine the radiation to a smaller solid angle, and the system which drives the sources into place. The detector has been modeled in details using the GEANT4 toolkit [61] which provides also the nuclear and electronic recoil differential cross-section. Using this powerful toolkit one simulates the response of the detector to the different sources and study the expected response of the detector.

## 4.1 Radioactive source

### 4.1.1 ER band calibration

Since the mean free path of  $\gamma$  traveling in xenon is of the order of several cm (8.3 cm for a 1 MeV  $\gamma$ ), depending on the  $\gamma$ 's energy 4.1, a good  $\gamma$  calibration source should emit energetic enough  $\gamma$ s to penetrate to the FV.

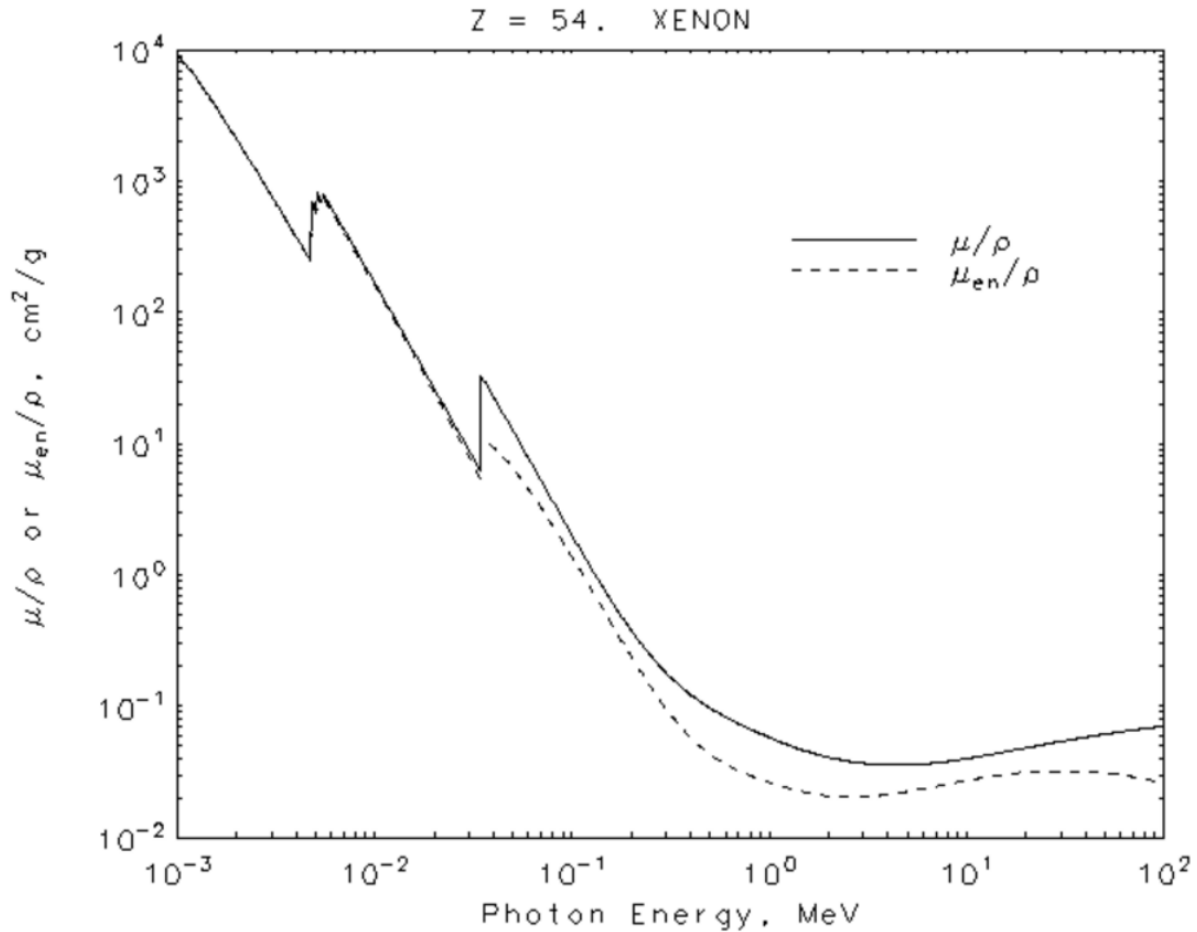
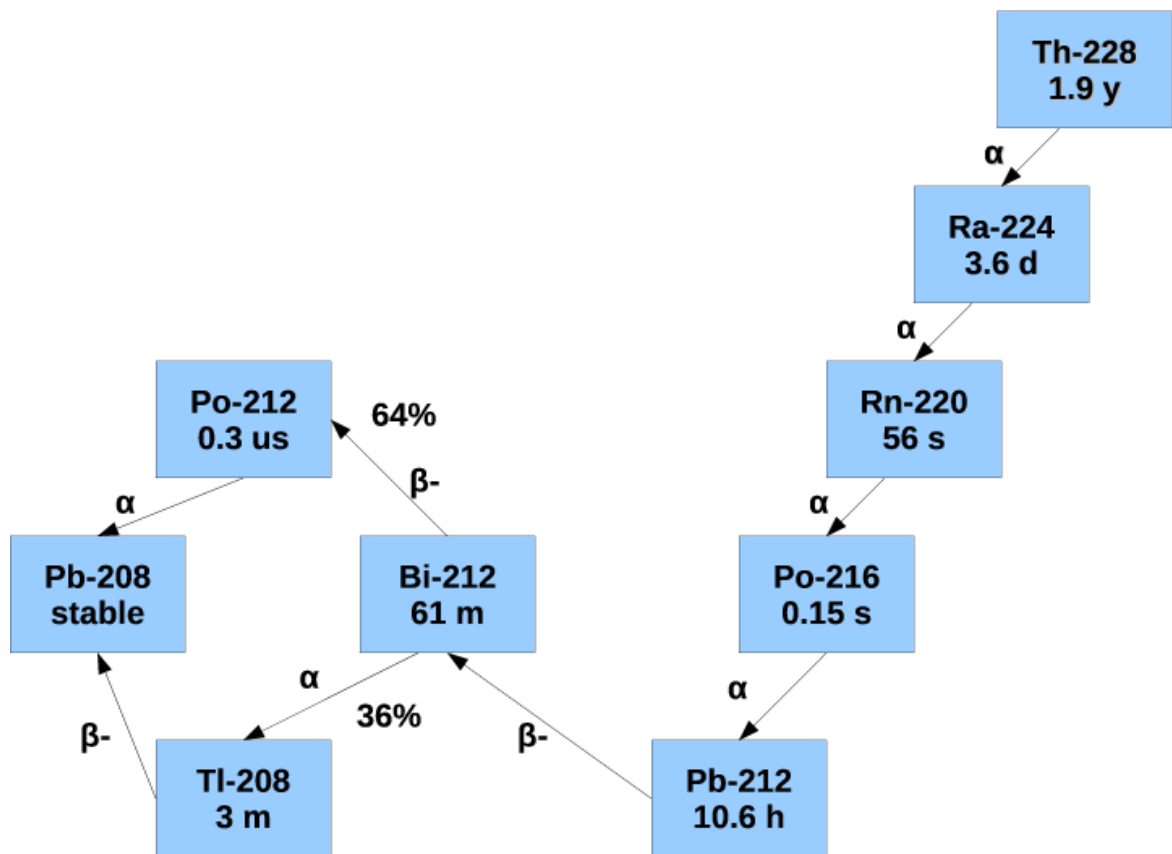


Figure 4.1: Attenuation coefficient of Xe. The relevant density for LXe is 3 g/cc.

After careful examination a  $^{228}\text{Th}$  source is selected, see decay chain is in Fig. 4.2 The source is encapsulated in SS and with an M4 thread. All  $\beta$  and  $\alpha$  decays will not reach the xenon because the source is encapsulated, leaving only  $\gamma$  radiation. The  $\gamma$  emission line for ER band calibration is the one coming from  $^{208}\text{Tl}$  with energy of 2614 keV and intensity of 99 %. Less energetic  $\gamma$  emission lines will penetrate the SV and trigger the PMTs but will not proceed to the FV and hence will be treated as background.

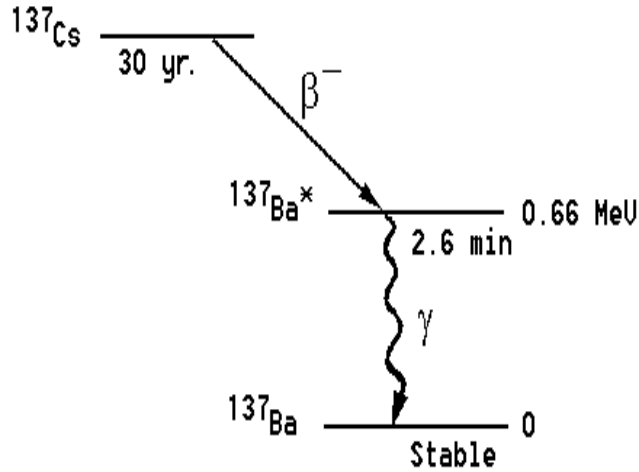
In order to estimate the percentage of good calibration events from total triggering all spectral lines are simulated, however only the 2614 keV events are considered as signal events, while the rest are treated as background. A summarize of the more energetic  $\gamma$  lines from  $^{228}\text{Th}$  decay chain is presented in Table 4.1.

All decays from  $^{208}\text{Tl}$  have an attenuation factor of 36% which is the branching ratio of  $^{212}\text{Bi} \rightarrow ^{208}\text{Tl}$ . In total the percentage of 2614 keV events in the SV is 0.69% of total source activity.

Figure 4.2:  $^{228}\text{Th}$  decay chain

Energy (keV)	SV prob(%)	Isotope	Intensity(%)
511	0.27	$^{208}\text{Tl}$	22.8
583	0.35	$^{208}\text{Tl}$	85
727	0.51	$^{212}\text{Bi}$	6.7
763	0.54	$^{208}\text{Tl}$	1.8
861	0.64	$^{208}\text{Tl}$	12.4
1621	1.15	$^{212}\text{Bi}$	1.5
2614	1.5	$^{208}\text{Tl}$	99

Table 4.1: High energy gamma lines from  $^{228}\text{Th}$  decay chain

Figure 4.3:  $^{137}\text{Cs}$  decay

#### 4.1.2 Charge collection efficiency

The calibration of the charge collection efficiency is done with less restrict data selection criteria than the ER band calibration. A good calibration sample for this calibration should have a well defined characteristic feature obtained from the source in various z-positions. By comparing the feature dependency on height a charge collection efficiency map is produced. An easy and well defined feature is the full absorption peak.

$^{137}\text{Cs}$  source which emits a 662 keV *gamma*, is selected for this calibration. The decay of  $^{137}\text{Cs}$  is shown in Fig 4.3. The source is deposited inside a 25 mm diameter disk.

## 4.2 Collimators

Large portion of the  $\gamma$ s arriving to the SV are scattered at the outskirts of the SV and don't reach the FV, these events trigger the PMTs however are of no use for ER band calibration. In order to lower this portion the gamma source will be placed behind a frame, with a conical hole, such that the solid angle of the hole will cover just the FV when the source is located at the center of the TPC (see Fig. 4.4).

There are two types of collimators: a 16X16X16 cm collimator which will just move vertically on a belt (I-Collimator), and a 10X10X10 cm collimator which passes below the cryostat (U-Collimator). Both collimators are made of Tungsten with a 45 deg aperture, sealed with a 1 mm SS plate to reduce the amount of water an emitted  $\gamma$  travels through. The two collimators are designed to host both threaded sources ( $^{228}\text{Th}$ ) and disk sources ( $^{137}\text{Cs}$ ). An M12 thread is located in front of the source position to allow adding an attenuator.

The collimators are attached to belts that drives them to various calibration positions. The

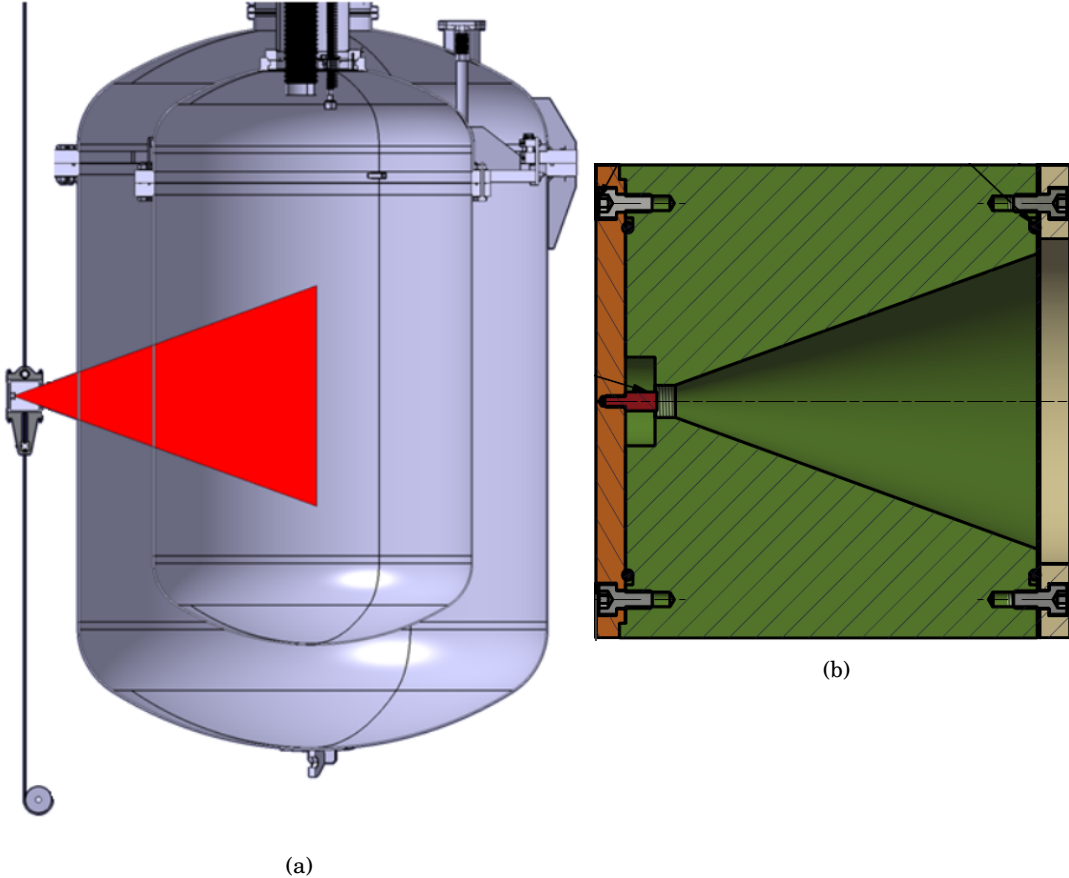


Figure 4.4: (a) The cryostat and the collimator shining just some of the FV (b) a CAD design of the collimator with the conical hole.

larger collimator is attached to an I-belt and moves only vertically, see Fig 4.5. The smaller collimator is attached to a U-belt, that passes below the cryostat, see Fig 4.5. The two I belts are connected to ports 5 and 11 while the U belt is connected to ports 12 and 7, on the water tank's top flange see Fig. 4.6

#### 4.2.1 Simulation

In order to decide the source activity and collimator dimensions, a MC simulation using the GEANT4 toolkit is used. The DAQ rate assumed for this study is 350 Hz. The response of the detector to 2614 keV $\gamma$ 's is simulated. Other  $\gamma$ 's coming from the detector are assumed to be background, and are considered only for rate calculations.

The results from the simulation of the I-Collimator which points to the center of the detector are shown in table 4.2, in Fig 4.7 are the original momentum-direction of  $\gamma$ s which do not produce a "good" calibration event. This is of importance to verify only events coming from the collimator



Figure 4.5: A picture of the two belts. The blue belt is the I-Belt (currently not the I-Belt in use). The grey belt is the U-Belt (with the U-Collimator mounted), which passes below the cryostat.

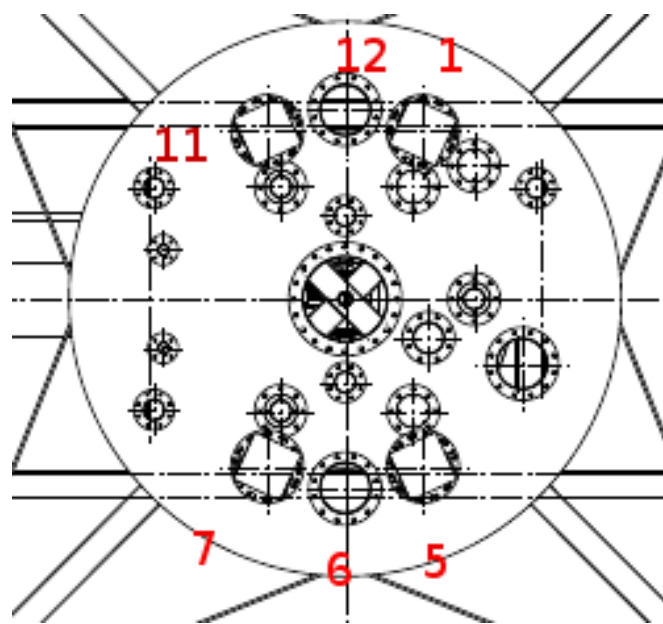


Figure 4.6: A top view of the water tank

number of simulated events	2e9
number of recorded events (SV)	2.5e7
number of good events	53
good evts/day @ 350Hz	65 ± 8
evt/day after bkg reduction	45

Table 4.2: result of GEANT4 simulations for a 16X16X16cm collimator with an aperture of 45 deg, a good event is an event that scattered only once in the FV with energy deposition of 2-15 keVee

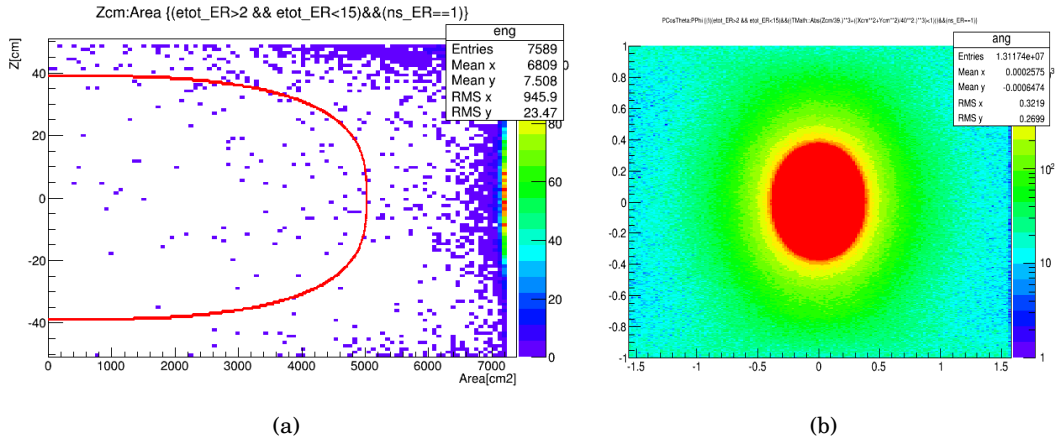


Figure 4.7: (a) scatter of good calibration events in the SV, the red line is the border of the FV (b) Intial momentum of background events i.e., events which trigger PMT's and do not meet all three conditions, FV, single scattered, and energy deposition range

opening will reach the detector's SV.

The detector is attached via a spring to the water tank's floor, this is done to apply force against the detector's buoyancy while filling water. Therefore the U-belt cannot pass underneath the center of the detector. This causes the collimator to be in a small angle with respect to the center of the detector. The results of the simulation of the U-Collimator are shown in table 4.3 and Fig. 4.8.

#### 4.2.2 First Results

number of simulated events	4e9
number of recorded events (SV)	4.05e7
number of good events	58
evt/day @ 350Hz good evts	$43 \pm 6$
evt/day after bkg reduction	30
Source activity	80kBq

Table 4.3: result of GEANT4 simulation for a 10X10X10cm collimator with an aperture of 45 deg, a good event is an event that scattered only once in the FV with energy deposition of 2-15 keVee

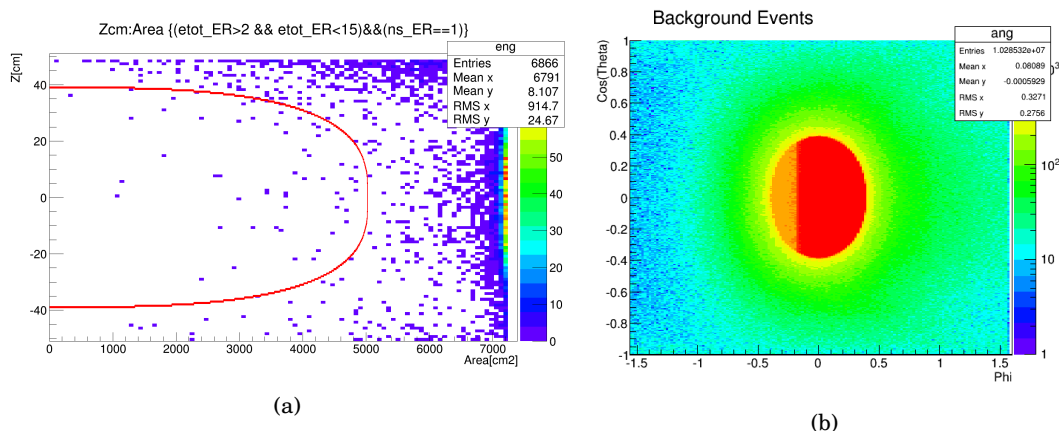


Figure 4.8: (a) scatter of good calibration events in the SV, the red line is the border of the FV (b) Intial momentum of background events i.e., events which trigger PMT's and do not meet all three conditions, FV, single scattered, and energy deposition range





## EFT SIGNAL MODEL DETECTOR RESPONSE TABLE

In this appendix digital tables which can be used to construct an accurate signal model for the EFT analysis given any input recoil spectrum  $dR/dE$  arising from a theoretical model is described. A visualization of the tables is shown in Fig. A.1.

The signal model for the high-energy analysis region can be expressed analytically in the form:

$$(A.1) \quad \frac{dR}{dcS1} = \int \frac{dR}{dE} \cdot \epsilon_{S1}(cS1) \cdot \epsilon_{S2'}(E) \cdot p_{S1}(cS1|E) dE$$

$$(A.2) \quad = \int \frac{dR}{dE} G(cS1, E) dE$$

where  $\epsilon_{S1}(cS1)$  and  $\epsilon_{S2'}(E)$  represent analysis cut efficiencies,  $p_{S1}(cS1|E)$  encodes detector effects, and  $dR/dE$  gives the theoretically predicted nuclear recoil rate from WIMP scattering. In the second line we emphasize that all the detector and analysis effects can be encoded in a single function  $G(cS1, E)$ . To make a signal prediction for the bins in our analysis, this expression needs to be integrated over the appropriate range of  $cS1$  for each bin (and divided by two to account for the banding structure in  $cS2_b$ ):

$$(A.3) \quad R_{bin_i} = \frac{1}{2} \int_{lower_i}^{upper_i} \frac{dR}{dcS1} dcS1$$

With some simple rearrangement this rate can be written in terms of an integral over the detector response function  $G$  as follows

$$(A.4) \quad R_{bin_i} = \frac{1}{2} \int \frac{dR}{dE} \int_{lower_i}^{upper_i} G(cS1, E) dcS1 dE$$

$$(A.5) \quad = \int \frac{dR}{dE} G'_i(E) dE$$

---

APPENDIX A. EFT SIGNAL MODEL DETECTOR RESPONSE TABLE

---

#	E(keV)	bin 1	bin 2	bin 3	bin 4	bin 5	bin 6	bin 7	bin 8	bin 9
3.00e+00	1.44e-22	2.70e-32	1.23e-42	0.00e+00	0.00e+00	0.00e+00	1.44e-22	1.23e-42	0.00e+00	
1.30e+01	9.21e-09	7.58e-14	1.25e-19	6.21e-40	0.00e+00	0.00e+00	9.21e-09	1.25e-19	0.00e+00	
2.30e+01	1.74e-04	1.07e-07	1.24e-11	1.51e-26	0.00e+00	0.00e+00	1.74e-04	1.24e-11	2.64e-32	
3.30e+01	2.22e-02	2.79e-04	6.56e-07	5.47e-18	8.20e-38	0.00e+00	2.25e-02	6.56e-07	1.71e-22	
4.30e+01	1.59e-01	1.68e-02	3.50e-04	1.89e-12	1.24e-28	1.82e-43	1.76e-01	3.50e-04	4.95e-16	
5.30e+01	2.23e-01	1.21e-01	1.40e-02	1.28e-08	6.89e-22	1.43e-34	3.44e-01	1.40e-02	1.82e-11	
6.30e+01	1.10e-01	2.12e-01	9.84e-02	4.73e-06	5.28e-17	5.47e-28	3.21e-01	9.84e-02	2.59e-08	
7.30e+01	2.77e-02	1.54e-01	2.51e-01	2.58e-04	2.20e-13	5.56e-23	1.82e-01	2.51e-01	4.20e-06	
8.30e+01	4.38e-03	6.14e-02	3.67e-01	4.07e-03	1.36e-10	5.26e-19	6.58e-02	3.71e-01	1.65e-04	
9.30e+01	4.65e-04	1.52e-02	3.96e-01	2.73e-02	2.31e-08	1.01e-15	1.57e-02	4.21e-01	2.44e-03	
1.03e+02	3.40e-05	2.47e-03	3.41e-01	9.81e-02	1.50e-06	6.05e-13	2.50e-03	4.21e-01	1.75e-02	
1.13e+02	1.91e-06	2.89e-04	2.29e-01	2.13e-01	4.09e-05	1.22e-10	2.91e-04	3.74e-01	6.77e-02	
1.23e+02	7.75e-08	2.38e-05	1.14e-01	3.28e-01	5.91e-04	1.16e-08	2.39e-05	2.76e-01	1.66e-01	
1.33e+02	2.18e-09	1.33e-06	3.98e-02	3.97e-01	5.03e-03	5.94e-07	1.33e-06	1.55e-01	2.87e-01	
1.43e+02	5.40e-11	6.21e-08	4.06e-02	4.21e-01	2.41e-05	1.42e-05	6.21e-08	6.64e-02	3.74e-01	
1.53e+02	1.33e-12	2.71e-09	2.23e-03	3.66e-01	7.14e-02	1.73e-04	2.71e-09	2.26e-02	4.17e-01	
1.63e+02	2.86e-14	1.00e-10	3.75e-04	2.85e-01	1.51e-01	1.32e-03	1.00e-10	6.04e-03	4.32e-01	
1.73e+02	5.43e-16	3.19e-12	5.09e-05	1.86e-01	2.43e-01	6.76e-03	3.19e-12	1.28e-03	4.34e-01	
1.83e+02	9.29e-18	8.90e-14	5.69e-06	1.01e-01	3.09e-01	2.42e-02	8.90e-14	2.21e-04	4.34e-01	
1.93e+02	1.44e-19	2.21e-15	5.32e-07	4.46e-02	3.23e-01	6.38e-02	2.21e-15	3.14e-05	4.31e-01	
2.03e+02	2.05e-21	4.92e-17	4.23e-08	1.62e-02	2.83e-01	1.29e-01	4.92e-17	3.73e-06	4.28e-01	
2.13e+02	2.71e-23	9.96e-19	2.91e-09	4.89e-03	2.10e-01	2.06e-01	9.96e-19	3.78e-07	4.21e-01	
2.23e+02	3.33e-25	1.85e-20	1.74e-10	1.23e-03	1.31e-01	2.71e-01	1.85e-20	3.29e-08	4.04e-01	
2.33e+02	3.83e-27	3.16e-22	9.25e-12	2.63e-04	6.94e-02	2.99e-01	3.16e-22	2.51e-09	3.69e-01	
2.43e+02	4.16e-29	5.03e-24	4.38e-13	4.80e-05	3.12e-02	2.81e-01	5.03e-24	1.68e-10	3.12e-01	
2.53e+02	4.29e-31	7.48e-26	1.87e-14	7.55e-06	1.20e-02	2.27e-01	7.48e-26	1.00e-11	2.39e-01	
2.63e+02	4.21e-33	1.05e-27	7.23e-16	1.04e-06	3.94e-03	1.58e-01	1.05e-27	5.38e-13	1.62e-01	
2.73e+02	3.95e-35	1.39e-29	2.56e-17	1.25e-07	1.12e-03	9.59e-02	1.39e-29	2.61e-14	9.70e-02	
2.83e+02	3.56e-37	1.74e-31	8.33e-19	1.34e-08	2.77e-04	5.04e-02	1.74e-31	1.15e-15	5.07e-02	
2.93e+02	3.08e-39	2.08e-33	2.51e-20	1.29e-09	6.00e-05	2.31e-02	2.08e-33	4.67e-17	2.31e-02	
3.03e+02	2.58e-41	2.38e-35	7.04e-22	1.11e-10	1.15e-05	9.25e-03	2.38e-35	1.75e-18	9.26e-03	
3.13e+02	2.03e-43	2.61e-37	1.84e-23	8.69e-12	1.95e-06	3.26e-03	2.61e-37	6.06e-20	3.26e-03	
3.23e+02	0.00e+00	2.76e-39	4.54e-25	6.20e-13	2.97e-07	1.01e-03	2.76e-39	1.96e-21	1.01e-03	
3.33e+02	0.00e+00	2.81e-41	1.05e-26	4.06e-14	4.06e-08	2.80e-04	2.81e-41	5.93e-23	2.80e-04	
3.43e+02	0.00e+00	2.72e-43	2.32e-28	2.44e-15	5.04e-09	6.91e-05	2.72e-43	1.69e-24	6.91e-05	

---

Table A.1: Detector response table using  $\mathcal{L}_{\text{eff}}$  with constrained scaling parameter set to  $-1\sigma$  value. First column gives recoil energies, subsequent columns give the values of  $G'_i(E)$  for each of the 9 high-energy analysis bins. The sampling is in steps of 10 keV<sub>nr</sub>, which is too coarse to give an accurate signal model for very low WIMP masses, but is suitable for the mass range most relevant to our analysis. Higher resolution  $G'_i(E)$  functions, and  $G'_i(E)$  functions for other values of  $\mathcal{L}_{\text{eff}}$ , are given in supplementary material.

where in the last line we absorb the factor of 1/2 into the definition of  $G'_i$ . We see here that the signal rate for each bin can be expressed as an integral over the recoil spectrum times a detector response function  $G'_i$  for that bin. It is these detector response functions which are shown in Fig. A.1, and which we provide digitally for use by the community. A low-resolution example is given in Table A.1. With these tables it is simple to produce a signal model for our analysis for any theoretical recoil spectrum. The functions  $G'_i$  are provided for three values of the nuisance variable  $\mathcal{L}_{\text{eff}}$ , namely the median value and values at  $\pm 1\sigma$  in  $\mathcal{L}_{\text{eff}}$ . From these, along with the measured background rates given in table 2.1, one may construct a likelihood which accounts for uncertainties in  $\mathcal{L}_{\text{eff}}$ . Alternatively simply using the  $-1\sigma$  value produces quite an accurate prediction and is generally conservative.

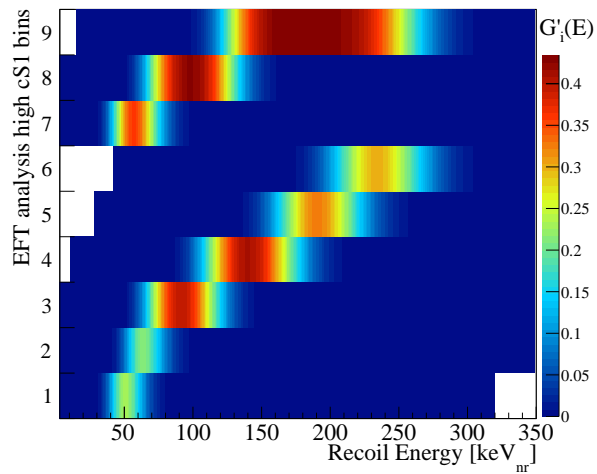


Figure A.1: A visualization of the detector response table for  $-1\sigma$  (i.e. conservative)  $\mathcal{L}_{\text{eff}}$ , as provided in the supplementary material. The y axis indicates the bins used for the high-energy signal region of this analysis (explained in 2.1). The x axis shows recoil energies, and the colors give the probability density for a recoil of a given recoil energy to produce an event in each analysis bin. To produce a signal model for this analysis, one simply multiplies the table values by  $dR/dE$  and integrates over  $E$ . The result is the predicted signal rate for each analysis bin.



## BIBLIOGRAPHY

- [1] K. Schneck *et al.*, “Dark matter effective field theory scattering in direct detection experiments,” *Phys. Rev.*, vol. D91, no. 9, p. 092004, 2015.
- [2] C. L. Bennett *et al.*, “Nine-Year Wilkinson Microwave Anisotropy Probe (WMAP) Observations: Final Maps and Results,” *Astrophys. J. Suppl.*, vol. 208, p. 20, 2013.
- [3] P. A. R. Ade *et al.*, “Planck 2015 results. XIII. Cosmological parameters,” *Astron. Astrophys.*, vol. 594, p. A13, 2016.
- [4] F. Zwicky, “On the Masses of Nebulae and of Clusters of Nebulae,” *Astrophys. J.*, vol. 86, pp. 217–246, 1937.
- [5] E. Aprile *et al.*, “XENON100 Dark Matter Results from a Combination of 477 Live Days,” *Phys. Rev.*, vol. D94, no. 12, p. 122001, 2016.
- [6] E. Aprile *et al.*, “First Dark Matter Search Results from the XENON1T Experiment,” 2017.
- [7] D. S. Akerib *et al.*, “Improved Limits on Scattering of Weakly Interacting Massive Particles from Reanalysis of 2013 LUX Data,” *Phys. Rev. Lett.*, vol. 116, no. 16, p. 161301, 2016.
- [8] A. Tan *et al.*, “Dark Matter Results from First 98.7 Days of Data from the PandaX-II Experiment,” *Phys. Rev. Lett.*, vol. 117, no. 12, p. 121303, 2016.
- [9] R. Agnese *et al.*, “Search for low-mass weakly interacting massive particles using voltage-assisted calorimetric ionization detection in the supercdms experiment,” *Phys. Rev. Lett.*, vol. 112, p. 041302, Jan 2014.
- [10] R. Bernabei *et al.*, “New results from DAMA/LIBRA,” *Eur. Phys. J.*, vol. C67, pp. 39–49, 2010.
- [11] M. Ackermann *et al.*, “Measurement of separate cosmic-ray electron and positron spectra with the Fermi Large Area Telescope,” *Phys. Rev. Lett.*, vol. 108, p. 011103, 2012.
- [12] M. Aguilar *et al.*, “First Result from the Alpha Magnetic Spectrometer on the International Space Station: Precision Measurement of the Positron Fraction in Primary Cosmic Rays of 0.5–350 GeV,” *Phys. Rev. Lett.*, vol. 110, p. 141102, 2013.

## BIBLIOGRAPHY

---

- [13] M. G. Aartsen *et al.*, “Improved limits on dark matter annihilation in the Sun with the 79-string IceCube detector and implications for supersymmetry,” *JCAP*, vol. 1604, no. 04, p. 022, 2016.
- [14] M. Aaboud *et al.*, “Search for dark matter at  $\sqrt{s} = 13$  TeV in final states containing an energetic photon and large missing transverse momentum with the ATLAS detector,” *Eur. Phys. J.*, vol. C77, no. 6, p. 393, 2017.
- [15] A. M. Sirunyan *et al.*, “Search for dark matter produced with an energetic jet or a hadronically decaying W or Z boson at  $\sqrt{s} = 13$  TeV,” *JHEP*, vol. 07, p. 014, 2017.
- [16] K. G. Begeman, A. H. Broeils, and R. H. Sanders, “Extended rotation curves of spiral galaxies: Dark haloes and modified dynamics,” *Mon. Not. Roy. Astron. Soc.*, vol. 249, p. 523, 1991.
- [17] V. C. Rubin, N. Thonnard, and W. K. Ford, Jr., “Rotational properties of 21 SC galaxies with a large range of luminosities and radii, from NGC 4605 /R = 4kpc/ to UGC 2885 /R = 122 kpc/,” *Astrophys. J.*, vol. 238, p. 471, 1980.
- [18] J. Silk *et al.*, *Particle Dark Matter: Observations, Models and Searches*. Cambridge: Cambridge Univ. Press, 2010.
- [19] A. Einstein, “Lens-Like Action of a Star by the Deviation of Light in the Gravitational Field,” *Science*, vol. 84, pp. 506–507, 1936.
- [20] I. Ferreras, P. Saha, and S. Burles, “Unveiling dark halos in lensing galaxies,” *Mon. Not. Roy. Astron. Soc.*, vol. 383, p. 857, 2008.
- [21] R. Gavazzi, T. Treu, J. D. Rhodes, L. V. Koopmans, A. S. Bolton, S. Burles, R. Massey, and L. A. Moustakas, “The Sloan Lens ACS Survey. 4. The mass density profile of early-type galaxies out to 100 effective radii,” *Astrophys. J.*, vol. 667, pp. 176–190, 2007.
- [22] N. Kaiser and G. Squires, “Mapping the dark matter with weak gravitational lensing,” *Astrophys. J.*, vol. 404, pp. 441–450, 1993.
- [23] D. Clowe, M. Bradac, A. H. Gonzalez, M. Markevitch, S. W. Randall, C. Jones, and D. Zaritsky, “A direct empirical proof of the existence of dark matter,” *Astrophys. J.*, vol. 648, pp. L109–L113, 2006.
- [24] S. W. Randall, M. Markevitch, D. Clowe, A. H. Gonzalez, and M. Bradac, “Constraints on the Self-Interaction Cross-Section of Dark Matter from Numerical Simulations of the Merging Galaxy Cluster 1E 0657-56,” *Astrophys. J.*, vol. 679, pp. 1173–1180, 2008.
- [25] R. D. Peccei and H. R. Quinn, “CP Conservation in the Presence of Instantons,” *Phys. Rev. Lett.*, vol. 38, pp. 1440–1443, 1977.

- [26] M. Pospelov and A. Ritz, “Electric dipole moments as probes of new physics,” *Annals Phys.*, vol. 318, pp. 119–169, 2005.
- [27] C. A. Baker *et al.*, “An Improved experimental limit on the electric dipole moment of the neutron,” *Phys. Rev. Lett.*, vol. 97, p. 131801, 2006.
- [28] J. E. Kim, “Weak Interaction Singlet and Strong CP Invariance,” *Phys. Rev. Lett.*, vol. 43, p. 103, 1979.
- [29] D. S. Akerib *et al.*, “First Searches for Axions and Axionlike Particles with the LUX Experiment,” *Phys. Rev. Lett.*, vol. 118, no. 26, p. 261301, 2017.
- [30] A. Manzur, A. Curioni, L. Kastens, D. N. McKinsey, K. Ni, and T. Wongjirad, “Scintillation efficiency and ionization yield of liquid xenon for mono-energetic nuclear recoils down to 4 keV,” *Phys. Rev.*, vol. C81, p. 025808, 2010.
- [31] E. Aprile *et al.*, “Measurement of the Scintillation Yield of Low-Energy Electrons in Liquid Xenon,” *Phys. Rev.*, vol. D86, p. 112004, 2012.
- [32] L. Baudis, H. Dujmovic, C. Geis, A. James, A. Kish, A. Manalaysay, T. Marrodan Undagoitia, and M. Schumann, “Response of liquid xenon to Compton electrons down to 1.5 keV,” *Phys. Rev.*, vol. D87, no. 11, p. 115015, 2013.
- [33] D. Muna, “The DRIFT-II directional dark matter detector,” *Nucl. Phys. Proc. Suppl.*, vol. 173, pp. 172–175, 2007.
- [34] C. Deaconu, M. Leyton, R. Corliss, G. Druitt, R. Eggleston, N. Guerrero, S. Henderson, J. Lopez, J. Monroe, and P. Fisher, “Measurement of the directional sensitivity of Dark Matter Time Projection Chamber detectors,” *Phys. Rev.*, vol. D95, no. 12, p. 122002, 2017.
- [35] R. Yakabe, Y. Yamaguchi, K. Miuchi, K. Nakamura, S. Nakaura, T. Hashimoto, T. Ikeda, and R. Taishaku, “Direction-Sensitive Dark Matter Search Using Micro Time-Projection-Chamber,” *JPS Conf. Proc.*, vol. 11, p. 040002, 2016.
- [36] Q. Riffard *et al.*, “MIMAC low energy electron-recoil discrimination measured with fast neutrons,” *JINST*, vol. 11, no. 08, p. P08011, 2016.
- [37] R. H. Dicke, “Coherence in spontaneous radiation processes,” *Phys. Rev.*, vol. 93, pp. 99–110, Jan 1954.
- [38] D. Rosenberger, “Superstrahlung in gepulsten argon-, krypton und xenon-entladungen,” *Physics Letters*, vol. 14, pp. 32–32, Jan. 1965.

## BIBLIOGRAPHY

---

- [39] J. D. Lewin and P. F. Smith, “Review of mathematics, numerical factors, and corrections for dark matter experiments based on elastic nuclear recoil,” *Astropart. Phys.*, vol. 6, pp. 87–112, 1996.
- [40] S. Chang, A. Pierce, and N. Weiner, “Momentum Dependent Dark Matter Scattering,” *JCAP*, vol. 1001, p. 006, 2010.
- [41] A. L. Fitzpatrick, W. Haxton, E. Katz, N. Lubbers, and Y. Xu, “Model Independent Direct Detection Analyses,” 2012.
- [42] N. Anand, A. L. Fitzpatrick, and W. C. Haxton, “Weakly interacting massive particle-nucleus elastic scattering response,” *Phys. Rev.*, vol. C89, no. 6, p. 065501, 2014.
- [43] A. L. Fitzpatrick, W. Haxton, E. Katz, N. Lubbers, and Y. Xu, “The Effective Field Theory of Dark Matter Direct Detection,” *JCAP*, vol. 1302, p. 004, 2013.
- [44] D. Tucker-Smith and N. Weiner, “Inelastic dark matter,” *Phys. Rev.*, vol. D64, p. 043502, 2001.
- [45] G. Barello, S. Chang, and C. A. Newby, “A Model Independent Approach to Inelastic Dark Matter Scattering,” *Phys. Rev.*, vol. D90, no. 9, p. 094027, 2014.
- [46] E. Aprile *et al.*, “Dark Matter Results from 225 Live Days of XENON100 Data,” *Phys. Rev. Lett.*, vol. 109, p. 181301, 2012.
- [47] E. Aprile *et al.*, “Analysis of the XENON100 Dark Matter Search Data,” *Astropart. Phys.*, vol. 54, pp. 11–24, 2014.
- [48] E. Aprile *et al.*, “The neutron background of the XENON100 dark matter search experiment,” *J. Phys.*, vol. G40, p. 115201, 2013.
- [49] E. Aprile *et al.*, “Response of the XENON100 Dark Matter Detector to Nuclear Recoils,” *Phys. Rev.*, vol. D88, p. 012006, 2013.
- [50] E. Aprile *et al.*, “Observation and applications of single-electron charge signals in the XENON100 experiment,” *J. Phys.*, vol. G41, p. 035201, 2014.
- [51] E. Aprile *et al.*, “Limits on spin-dependent wimp-nucleon cross sections from 225 live days of xenon100 data,” *Physical review letters*, vol. 111, no. 2, p. 021301, 2013.
- [52] G. Cowan, K. Cranmer, E. Gross, and O. Vitells, “Asymptotic formulae for likelihood-based tests of new physics,” *Eur. Phys. J.*, vol. C71, p. 1554, 2011. [Erratum: Eur. Phys. J.C73,2501(2013)].
- [53] E. Aprile *et al.*, “Dark Matter Results from 100 Live Days of XENON100 Data,” *Phys. Rev. Lett.*, vol. 107, p. 131302, 2011.

---

## BIBLIOGRAPHY

- [54] E. Aprile *et al.*, “Likelihood Approach to the First Dark Matter Results from XENON100,” *Phys. Rev.*, vol. D84, p. 052003, 2011.
- [55] A. L. Read, “Modified frequentist analysis of search results (The CL(s) method),” in *Workshop on confidence limits, CERN, Geneva, Switzerland, 17-18 Jan 2000: Proceedings*, pp. 81–101, 2000.
- [56] Z. Ahmed *et al.*, “Dark Matter Search Results from the CDMS II Experiment,” *Science*, vol. 327, pp. 1619–1621, 2010.
- [57] D. Yu. Akimov *et al.*, “Limits on inelastic dark matter from ZEPLIN-III,” *Phys. Lett.*, vol. B692, pp. 180–183, 2010.
- [58] E. Aprile *et al.*, “Implications on Inelastic Dark Matter from 100 Live Days of XENON100 Data,” *Phys. Rev.*, vol. D84, p. 061101, 2011.
- [59] A. De Simone and T. Jacques, “Simplified models vs. effective field theory approaches in dark matter searches,” *Eur. Phys. J.*, vol. C76, no. 7, p. 367, 2016.
- [60] N. G. Basov, V. A. Danilychev, and Y. M. Popov, “Stimulated emission in the vacuum ultraviolet region,” *Soviet Journal of Quantum Electronics*, vol. 1, no. 1, p. 18, 1971.
- [61] S. Agostinelli *et al.*, “Geant4 a simulation toolkit,” *Nuclear Instruments and Methods in Physics Research Section A: Accelerators, Spectrometers, Detectors and Associated Equipment*, vol. 506, no. 3, pp. 250 – 303, 2003.

